Fabrication, Characterization, and Micromagnetic Analysis of Lithographically Defined Particle Arrays for Applications in Data Storage

by

Minha Hwang

B.S. Metallurgical Engineering

Seoul National University, 1994

Submitted to the Department of Materials Science and Engineering
in partial fulfillment of the requirements for the degree of

Doctor of Philosophy

at the

MASSACHUSETTS INSTITUTE OF TECHNOLOGY

June 2001

Author .....
Department of Materials Science and Engineering
May 3, 2001

Certified by .....
Caroline A. Ross
Associate Professor of Materials Science and Engineering
Thesis Supervisor

Accepted by .....
Harry L. Tuller
Professor of Ceramics and Electronic Materials
Chair, Departmental Committee on Graduate Students

FABRICATION, CHARACTERIZATION, AND MICROMAGNETIC ANALYSIS OF LITHOGRAPHICALLY DEFINED PARTICLE ARRAYS FOR APPLICATIONS IN DATA STORAGE

by

Minha Hwang

Submitted to the Department of Materials Science and Engineering
on May 3, 2001, in partial fulfillment of the
requirements for the Degree of Doctor of Philosophy in
Materials Science and Engineering

Abstract

In this thesis, the magnetic behavior of nanostructured ferromagnetic particle arrays are studied by experiments and numerical micromagnetics for ultra-high-density data storage applications. 100nm or 200nm period arrays of nanostructured nickel, cobalt, and cobalt phosphorus are fabricated by the techniques of interference lithography combined with evaporation and electrodeposition. The nanomagnet arrays are characterized by bulk magnetometry and magnetic force microscopy. The remanent states of evaporated conical particles and electrodeposited cylindrical particles are studied by micromagnetic simulations and compared with experimental measurements. For electrodeposited particles, the influence of size, aspect ratio and microstructure on switching field is also investigated. Finally, the effect of demagnetizing magnetostatic interactions and switching field spread on the squareness and the shape of hysteresis loops is studied with the help of an Ising-like interaction model. Based on these observations, a stability condition for patterned media is found and used for determining the optimum spacing between nanomagnets.

Thesis Supervisor: Caroline A. Ross
Title: Associate Professor of Materials Science and Engineering

Table of Contents

List of Figures

List of Tables

Acknowledgement

There have been so many people who have helped me throughout the course of my study at MIT. I am deeply grateful first and the most to my advisor, Prof. Caroline Ross. Caroline has been the best advisor that anyone could hope for. She has been a great mentor, an engineer, and a teacher. Her patience, ingenuity, kindness and passion for science really have inspired me during my years here. I will never forget her support and encouragement especially when I was struggling with emotional fluctuations. She has been a good role model for me and the lessons I learned from her during my stay here will carry over throughout my life.

I would like to thank Dr. Makhlouf Redjdal and Prof. Floyd Humphrey at BU for guiding me through the world of numerical micromagnetics. Collaboration with these great micromagneticians enabled me to make a breakthrough in my research. Simulation on switching field could not have been performed without the help of Dr. Chris Seberino, who taught me how to run simulations in a parallel computing environment such as a Intel linux cluster or Cray T3E, and Prof. H Neal Bertram at UCSD, who kindly invited me over to San Diego for the training. They helped me to understand numerical micromagnetics better.

My special thanks go to friends of the Ross research group. I have extensively worked with Dr. Maya Farhoud for most of my time at MIT. Her fabrication and characterization expertise made much of this work possible. I have learned greatly from her and would like to extend my sincere gratitude to her. It was great to have Dr. Douglas Twisselmann, who graduated 6 months ago, in our group. I have been constantly impressed by his optimistic ways of thinking and his wit and humor made my stay more enjoyable. Dr. Mutsuhiro Shima taught me a great deal about electrodeposition of cobalt and cobalt phosphorous. I am always amazed by his diligence and passion for science. He showed me a good example of a dedicated researcher. Other members of the group, Joy Cheng, Yaowu Hao, Fernando Castano, Bernard Vogeli, Mike Walsh, Ellen Siem, Susumu Haratani, Elizabeth Lyons, and Peter Chamber also deserves recognition for helping my in many ways during my years here. Your friendship meant a lot to me.

My sincere thanks also go to members of my thesis committee, Prof. Rose, Prof. Smith, and Dr. Bob O'handley for all their useful comments regarding this thesis.

Outside my research group, I thank nanofabrication experts of the Nanostructures Laboratory. Jimmy Daley, Jim Carter, Tim Savas, Mike Walsh, and Mark Mondol taught me innumerable things about nanofabrication and characterization techniques. Mathew Abraham in Prof. Rajeev Ram's group trained me on magnetic force microscopy measurements in my early days. Discussion with Dr. Holdger Schmidt was also helpful to understand my subject better.

I spent many study hours with Kevin Lee, Jinsang Kim, Cheolmin Park, and Jinwoo Park (the "Eagle Five") especially in my first year. I have benefited greatly from discussions and our group study at Hayden. Kevin Lee has been the best studymate, as well as a good

friend. We spent much time together at school, at home, and at church. I am hoping that our paths will cross again in the future. Jinwoo Park has been a wonderful counselor for numerous worries that bothered me. Her advice and care meant so much to me. My friends at KCCB have made my time in Boston full of memory and great moments. My friendship with Sanghoon Ahn, Eunji Seo, Kevin Lee, Youngjoo Jeon, Jungkyu Kwon, Inkyung Kim, Taekjin Choi, Michael Song, Hyun Ryu, Naeeun Lee, Heesun Kim, Hoon Kim, Hongsik Kim, Paul Lee, Joonyoung Lee, Jaeeun Jung, Jooyong Kim, Heung Soo Kim, Kyunghwa Lee, and Sangwon Kang is sure to last throughout my life.

I also thank my fellow graduate students and friends who have made my years at MIT so pleasant. Dongwon Choi, Taesoon Park, Seonah Lee, Songyee Yoon, Jiyoon Kim, Joon Chae, Donghwan Lee, Jinwook Lee, Yongki Min, Taeshin Park, Sungjee Kim, Wonseon Choi, Heejae Kim, Joosoo Lee, and many others, they all have been an important part of my life at MIT and made a difference. Their friendship will always be treasured.

Finally, I would like to thank my loving family. I wouldn't make it through without their continued support and encouragement. I am really grateful for their love and care.

Chapter 1

Introduction

Section 1.1 describes the history of the hard drive and its impact on data storage as a background. Motivation for the thesis is delivered in Section 1.2. The goals of this work are given in Section 1.3. Section 1.4 discusses the history and the critical role of micromagnetic modeling. Section 1.5 concludes Chapter 1 with the outline of the thesis.

1.1 Background

1.1.1 History of the Hard Disk

Hard disk storage is one of the most important components of the storage hierarchy in modern computers due to its nonvolatility and low cost per megabyte. Since IBM introduced the first computer disk storage system in 1956, the Random Access Method of Accounting and Control (RAMAC), the areal density of hard disks has been increased enormously and the price per megabyte has dropped significantly. In general, densities and data rates have doubled every three years [1]. Since 1991, the areal density of hard disks has increased at a rate of 60% per year, and since 1997, it has doubled every year [2]. This acceleration of growth is due to the introduction of the magnetoresistive (MR) recording head by IBM, an increase of competition in the marketplace, and a transfer of technological leadership to small-diameter drives with shorter design cycles [2]. Moreover, there are greater demands for high performance data storage systems in recent years. Specifically, with the advent and prevalence of high performance personal computers, Internet, and digital audio/video technologies, storage systems with densities of more than several hundred Gbytes need to be built. Customers are willing to spend money for better data storage if the cost is not too high. It is shown that each 1% decrease in price is accompanied by 4% increase in demand [3].

Today, a megabyte in a hard disk costs only $0.02. Data transfer rate of 60Mbytes/s have been realized with high areal densities and disk rotation of 10,000 RPM [4]. Through the use of advanced actuator designs and improved, lighter materials, the access time is now about 9 milliseconds [4]. A 17.2 Gbits/in^2 hard drive (IBM's Travelstar 30GT) is available on the market, and researchers presented laboratory demonstrations of 65 Gbits/in^2 in 2001. However, many researchers believe that increases beyond 200 Gbits/in^2 will be limited by the thermal instability, or superparamagnetism, of grains comprising the Co-alloy based thin film media. The detailed explanation for this phenomena is given in the following section.

1.2 Motivation: Superparamagnetic Limit

Conventional hard disk media is commonly made by sputtering a Cr underlayer and a Co-alloy magnetic layer onto a substrate made of nickel-phosphorus (NIP)-plated aluminum. The Co-alloy layer is polycrystalline with the grains or 'particles' on the order of 10-15nm in diameter in the film plane (Figure. 1.1). The grain easy axes (Co [0002] axis) are random in the plane and the grains are magnetically exchange decoupled due the preferential Cr segregation around the grain boundaries. Since each grain is small enough to be a single-domain particle, the thin-film media can be thought as a collection of weakly coupled uniaxial single-domain particles. Data is recorded by applying a magnetic field with an inductive head, magnetizing a cluster of grains, called a bit cell. Read-back is achieved by sensing the fringing field between two oppositely magnetized, neighboring bit cells. Since only the average magnetization value over the bit-cell is measured, each bit cell must be comprised of at least 1000 grains to give a reasonable signal-to-noise ratio (*S/N*), which is proportional to the square root of the number of grains in each bit cell. To increase the areal density of a hard disk, the bit cell size should be decreased, which means the grain

size has to be refined while maintaining the number of grains per each bit.

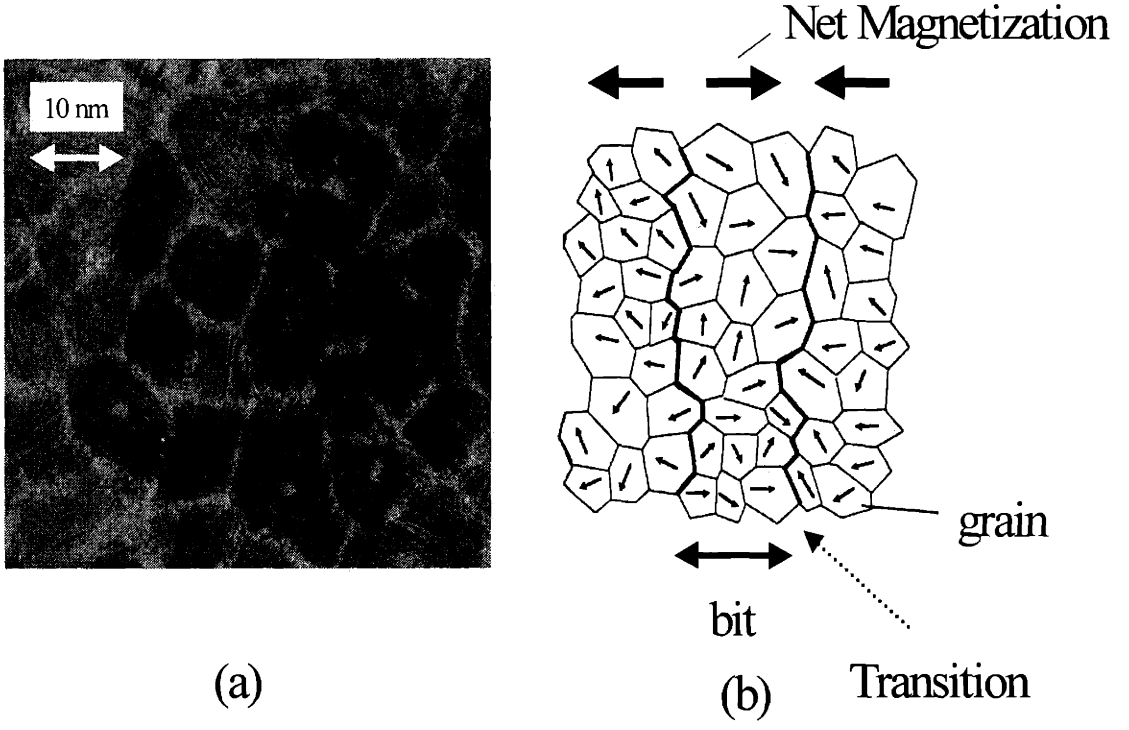

Figure 1.1: (a) TEM image of typical polycrystalline thin film conventional media. Taken from M. Doerner et al [5]. (b) Schematic of written magnetic transition. Bits are represented as transitions between regions of opposite net magnetization. Each bit is composed of hundreds of single-domain grains [6].

Heretofore, the areal density growth has been possible through a scaling down of both bit-cell size and grain size, but if grains become too small, the thermal energy (k_BT) can reverse their magnetization direction, which means that we can not use these grains for data storage any longer. Each grain can exist in one of two equivalent states of opposite magnetization, and occupies one state, depending on its past history. These two energy minima are separated by an energy barrier with a magnitude KV, where K is the magnetic anisotropy energy density of the grain and V is the grain volume (Figure 1.2). A grain's average magnetic reversal time (in seconds) is given by:

$$\tau^{-1} = f_0 e^{\frac{-KV}{k_B T}} \tag{1.1}$$

where f_0 is a constant, which has a dimension of frequency. The original estimation of Neel was $f_0 = 10^9\ s^{-1}$, but it has recently become more customary to take $f_0 = 10^{10}\ s^{-1}$ [7].

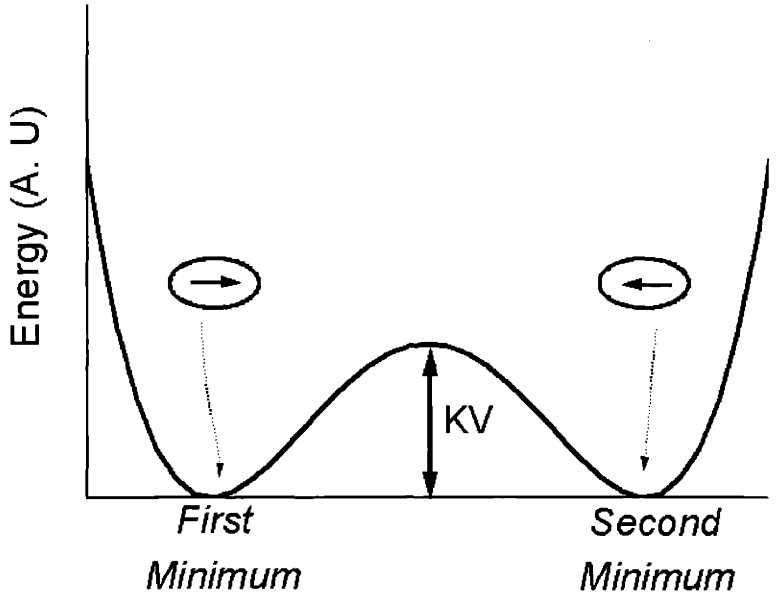

Figure 1.2: The energy barrier between bi-stable states of single-domain grain with zero applied field. The arrow inside the grain represents the magnetization direction within the single-domain grain.

The dependence of the average reversal time on the ratio V/T is extremely large. For example, if we take $K \sim 3.9 \times 10^6$ ergs/cm^2 (the magnetocrystalline anisotropy constant of cobalt) with the Neel value of $f_0 = 10^9\ s^{-1}$ and assume $T \sim 300$K, we find that τ changes from 1.08×10^5 s to 1.3×10^{-4} s when $V^{1/3}$ changes from 7nm to 5nm. The particle of 7nm

size appears to be permanently magnetized in a fixed direction over usual measurement times, whereas the particle of 5nm size oscillates between two opposite magnetizations so rapidly that on the measurement time scale, it would appear to have a magnetization value of zero. This particle resembles paramagnetic particles since its net magnetization is zero under the absence of the magnetic field; this type of behavior is called superparamagnetism. The transition between these two extrema depends on the time scale of interest, but an energy barrier of $25k_BT$, which gives average reversal times on the order of a few seconds is commonly chosen as a transition value. For data storage applications, information has to be kept for years, so we use larger value for the thermal stability in hard disk media. Moreover, in hard disk media, the demagnetization field from neighboring bits lowers the effective barrier height, so $60k_BT$ is used as an acceptable barrier height. Grain diameters and film thicknesses currently range between 10 - 20nm, leaving little opportunity for decreasing grain volume while retaining thermal stability. Decreases in grain volume could be compensated by increases in K, but with high values of K, it becomes more difficult to write the data on the medium. The maximum field that a writing head can produce is about 5000 Oe [8]; hence, there is certainly a limit for the increase of the anisotropy. Recently, researchers at IBM demonstrated an antiferromagnetically coupled media (AFC media), in which V is effectively increased while maintaining $M_r t$ (M_r: remanent magnetization, t: thickness of the film) and S/N [5], but it seems that this enables at most a two-fold to four-fold increase in areal density. More drastic measures to attack this fundamental physical limit have to be taken, and patterned discrete media, which is one of the most promising solutions, will be explained in the following section.

1.3 Goals: What patterned media can do for high density storage

1.3.1 Patterned Media: 200 Gbits/in^2 and Beyond

The concept of lithographically patterning a hard disk was originally introduced to improve head tracking and *S/N*, but it is now clear that patterning offers the possibility of much higher areal densities than conventional hard disk media [6,9,10]. A patterned medium consists of a periodic array of discrete elements or "nanomagnets." Each element is a single domain magnetic particle, with uniaxial magnetic anisotropy so that the magnetization of the element points in one of only two possible directions at remanence, representing 1 bit of data. Each element can be a single crystal or polycrystalline. For polycrystalline structures, grains are strongly coupled to one another, so they respond to a magnetic field in a collective way, contrary to conventional hard disk media. So, for thermal stability considerations in patterned media, not grain size but element size is relevant. A schematic of patterned media is illustrated in Figure 1.3. The maximum achievable density depends on the size of particles (which controls thermal stability) and the period of particle arrays (which controls magnetostatic interaction). With a 10nm particle size and 25nm period, ultra-high densities of 1 Tbits/in^2 could be achievable. Since we are dealing with strongly-coupled grains, we do not need many grains per bit for a high *S/N*, and that is why we can scale down bit size much further than in conventional hard disk media. There are two schemes to align the magnetic easy axis. The magnetic anisotropy axis can lie either parallel to the plane, as in longitudinal thin-film media, or perpendicular to the plane, as in perpendicular media. Since higher areal density would be achievable with perpendicular media due to advantages with respect to "self-demagnetization," only perpendicular media is considered in this work.

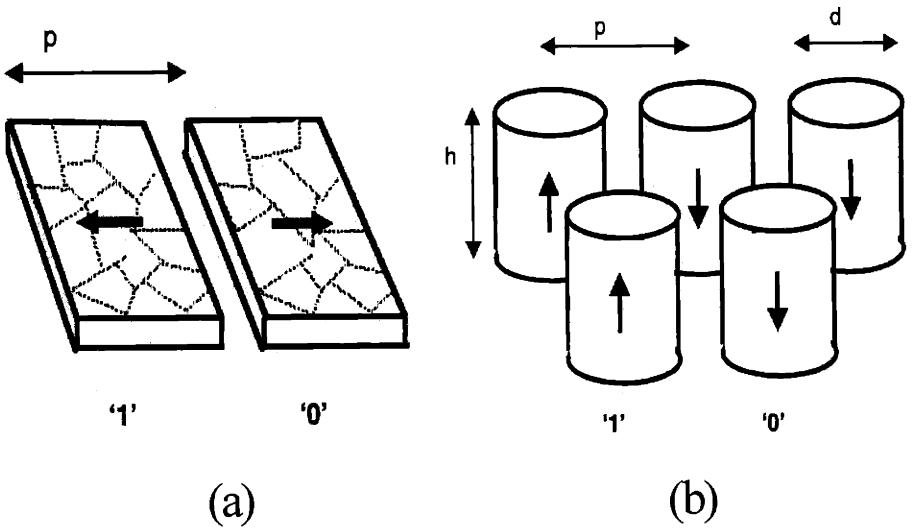

Figure 1.3: (a) Patterned medium with in-plane magnetization. Bits are lithographically defined and have period p. (b) Patterned medium with out-of-plane magnetization. The height is *h*, the diameter *d*, and the period *p*. Bi-stable states are shown as '1' and '0'. Figures are taken from [6].

1.3.2 .Goals of the Research

Studies of the magnetic properties of single-domain particles and their potential applications in magnetic storage have been a challenge for decades and have prompted intense research activity. The literature is rich with both fabrication schemes and theoretical micromagnetic studies, but few researchers have attempted to directly compare experiments with theoretical predictions. This fact is due mainly to the lack of control over the sample geometry on the fabrication side, and lack of computing power on the simulation side. Experimentally, assemblies of small ferromagnetic particles have been made by a range of techniques, but the behavior of the assemblies has been difficult to model because of the variability in the sizes, shapes, and spacings of the particles. Theoretically, the mis-

match between the size of real samples and the size for which three-dimensional numerical micromagnetic calculations are possible have made finding a model system for the simulation results quite difficult.

Recent advances in both lithography techniques and computing power allow us to now correlate the experimental results with theoretical predictions, thus opening the possibility of applying computations to design and optimization of nanomagnet arrays for data storage. The goal of this work is to perform a comprehensive study of single-domain particle arrays in order to discover what the design rules for the patterned media are. This is summarized below.

(1) By using a versatile nanolithography technique, we have made prototype patterned media with particles of different sizes, shapes, and materials, and characterized them with magnetometries and conventional structural characterization tools.

(2) With the help of a micromagnetic simulation and a model of magnetostatic interaction, the effect of control parameters (diameter, height, shape, saturation moment, and anisotropy constant of particles) on magnetic properties of particle arrays is calculated and compared with experimental results.

(3) From these experimental and theoretical findings, we make design and optimization rules for ideal patterned media.

1.4 Micromagnetic Modeling and Its Critical Role for Design

Since the fabrication and characterization of samples is quite time-intensive and difficult, micromagnetic modeling can be an useful tool for designing and optimizing patterned media if it can be experimentally verified. A larger parameter space can be studied in a controlled way through numerical experiments, which gives valuable insights for making improved media. Micromagnetics is a phenomenological model based on continuum theory. It searches for magnetization distributions with the lowest total energy. In a ferromagnetic particle systems, there are four types of free energy: magnetic anisotropy energy which is magnetocrystalline in origin; exchange energy due to spin-spin exchange coupling; magnetostatic energy due to dipole interaction among elements; and Zeeman energy due to an external field. With a given field history, an equilibrium magnetization configuration is computed at each field, which gives figures of merit (FOM) for the media, such as remanence, squareness, coercivity (switching field), and so on. The details will be given in Chapter 2.

1.5 Thesis Outline

This thesis is organized as follows. In Chapter 2, the micromagnetic model and the calculation methodology are presented. In Chapter 3, details of sample fabrication and characterization methods are given. In Chapter 4, experimental results on evaporated conical particles are compared with micromagnetic simulation results. Chapter 5 is divided into two parts. In the first part, experimental results for individual electrodeposited cylindrical particle are compared with micromagnetic simulation results. Based on the properties of

single particles, the collective behavior of particle arrays is analyzed in the second part. The effect of magnetostatic interactions on the magnetic properties of particle arrays is addressed with the help of an interaction model. Finally, patterned media design criteria are summarized. Chapter 6 concludes this thesis by giving a summary and discussing the limitation and barriers for real implementation. All equations and magnetic parameters are reported in cgs units in this thesis.

Chapter 2

Micromagnetic Model and Computation

2.1 Micromagnetics: Methodology and Governing Equations

In micromagnetics, magnetization is represented by a continuous function of position. Magnetization is assumed to have a constant magnitude M_s but can vary its direction from point to point. For given material parameters and external field, the magnetization configuration of minimum total free energy is sought, based on a variational principle. Except for ideal shapes such as ellipsoids or an infinite cylinder, it is hard to analytically solve these problems, so numerical schemes are used in general. The micromagnetics method is based on two governing equations, depending on whether we are interested in equilibrium magnetization spin configuration or dynamic evolution of the spin system. Brown's equation is derived from the energy minimization of a spin system. Each individual spin is subject to the action of the torque due to internal forces such as exchange, anisotropy, magnetostatic interaction, and external field. The vector torque per unit volume,

$$\vec{L} = \vec{M} \times \overrightarrow{H_{eff}} \tag{2.1}$$

should be zero everywhere in the sample volume. Here $\vec{M}$ is the magnetization vector at each point and $\overrightarrow{H_{eff}}$ is the local effective field obtained by adding up contributions from all internal forces described above. The equilibrium state is reached when the magnetization at any point aligns itself in the direction of the local field, thus making the torque per unit volume vanish everywhere. The dynamic behavior of the spin system can be described by:

$$\frac{\partial}{\partial t}\vec{G} = \vec{L} \tag{2.2}$$

where $\vec{G}dv$ is the angular momentum associated with the magnetic moment $\vec{M}dv$. According to quantum theory, the magnetic moment $\vec{M}$ is proportional to its angular momentum $\vec{G}$,

$$\vec{G} = \gamma\vec{M} \tag{2.3}$$

where γ is the gyromagnetic ratio. Combining Eq. 2.1, Eq 2.2, and Eq. 2.3 gives the equation of motion for the magnetization,

$$\frac{\partial}{\partial t}\vec{M} = \gamma\vec{M}\times\vec{H}_{eff} \tag{2.4}$$

This equation means that a magnetization vector precesses indefinitely around the effective field. In real ferromagnetic materials, the magnetization vector eventually aligns itself along the direction of the field due to the existence of dissipation (damping). This damping can be treated by subtracting from $\vec{H}_{eff}$ a phenomenological term that is proportional to $\frac{\partial}{\partial t}\vec{M}$. The equation of motion is then changed to,

$$\frac{\partial}{\partial t}\vec{M} = \gamma\vec{M}\times\left(\vec{H}_{eff}-\eta\frac{\partial}{\partial t}\vec{M}\right) \tag{2.5}$$

which is given by Gilbert in 1955 [11]. Here η is a positive constant. This formulation is equivalent to the older form given by Landau and Lifshitz in 1935 [12], which is,

$$\frac{\partial}{\partial t}\vec{M}=\gamma\vec{M}\times\vec{H}_{eff}-\frac{\alpha\gamma}{M_s^2}\vec{M}\times(\vec{M}\times\vec{H}_{eff}) \tag{2.6}$$

where M_s is the saturation moment, γ and α are, respectively, the gyromagnetic ratio, and damping coefficient.

2.2 Energy Density: General Formulation

To solve these governing equations of motion, we have to first evaluate $\overrightarrow{H_{eff}}$, which is given by,

$$\vec{H}_{eff} = \frac{\partial E_{total}}{\partial \vec{M}} \tag{2.7}$$

where E_{total} is the total energy density. The total magnetic energy, E_{total} can be written as,

$$E_{total} = E_{app} + E_{an} + E_{ex} + E_d \tag{2.8}$$

where E_{app} is the Zeeman energy from an externally applied field, E_{an} is the crystalline anisotropy energy, E_{ex} is the exchange energy, and E_d is the magnetostatic interaction energy. A detailed description and the explicit integral form of each energy term will be given in the following subsections.

2.2.1 Zeeman Energy

The Zeeman energy term is due to an externally applied field and often called magnetic potential energy. It is minimized when the magnetization vector lies along the direction of the applied field. The energy is given by,

$$E_{app} = -\int_V \vec{H}_{ext} \bullet \vec{M} dV \tag{2.9}$$

where $\vec{H}_{ext}$ is the external applied field and the integration is carried out over the volume of the system. The applied field and magnetization can vary from point to point.

2.2.2 Anisotropy Energy

The energy of a ferromagnet depends on the direction of the magnetization relative to crystalline axes of the material. This dependence, which is due to spin-orbit interactions, is phenomenologically described by the anisotropy energy. Expansions in terms of spherical harmonics are used to describe the most important contribution [13]. Since we are dealing with nickel or cobalt particles in this study, expressions only for cubic (Ni) and uniaxial (Co) symmetries are given below. The crystalline anisotropy energy can be written as

$$E_{an} = \int_V u_{an}(\vec{m})dV \tag{2.10}$$

where $u_{an}(\vec{m})$ is some spherical harmonic expansion depending on the symmetry of the system and $\vec{m} = \frac{\vec{M}}{M_s}$ is the normalized magnetization density vector. For the uniaxial case,

$$u_{an}(\vec{m}) = K_{u1}\sin^2\theta + K_{u2}\sin^4\theta \tag{2.11}$$

where θ is the angle between the anisotropy axis and magnetization direction and Ku_1/ Ku_2 are uniaxial anisotropy constants from measurements on single crystal samples. For cubic crystals,

$$u_{an}(\vec{m}) = K_{c1}\left(\alpha_1^2\alpha_2^2 + \alpha_1^2\alpha_3^2 + \alpha_2^2\alpha_3^2\right) + K_{c2}\alpha_1^2\alpha_2^2\alpha_3^2 \tag{2.12}$$

where α_1, α_2, and α_3 are projections of unit magnetization vector $\vec{m}$ on the three crystalline easy axes and Kc_1/ Kc_2 are material constants from measurements on single crystal samples.

2.2.3 Exchange Energy

The fundamental property of a ferromagnet is its preference for an alignment of neighboring spins. Deviations from this alignment cause an energy penalty, which can be described by,

$$E_{ex} = \int_V A(\nabla \vec{m})^2 dV \tag{2.13}$$

where A is a material constant, called the exchange stiffness constant.

2.2.4 Magnetostatic Interaction Energy

The magnetostatic interaction energy is due to the magnetic field generated by the magnetic body itself. The magnetostatic interaction energy can be written as,

$$E_d = -\frac{1}{2}\int \vec{H}_D \bullet \vec{M} dV \tag{2.14}$$

where $\vec{H}_D$ is the demagnetizing field due to the magnetostatic surface and volume charges. The magnetostatic volume charges, λ_v are given by $-div\vec{M}$ and the magnetostatic surface charges, σ_s are given by $\hat{n} \bullet \vec{M}$, where $\hat{n}$ is the outward surface normal vector. With the help of potential theory, the scalar potential of the stray field at position $\hat{r}$ can be written as an integration over $\hat{r}'$. From $\overrightarrow{H_D} = -\nabla\Phi(\hat{r})$, we can derive the demagnetizing field,

$$\Phi(\hat{r}) = \left[\int \frac{\lambda_s(\hat{r}')}{|\hat{r} - \hat{r}'|} dV + \int \frac{\sigma_s(\hat{r}')}{|\hat{r} - \hat{r}'|} dS \right] \tag{2.15}$$

The magnetostatic interaction energy calculation can be a six-fold integration when dealing with a 3-dimensional body; it is the most difficult micromagnetic term to evaluate.

2.3 Numerical Calculation Method

The general formulations above can only be solved for the case of simple and idealized shapes such as an ellipsoid, where linear approximations are possible [13,14,15,16]. Our prototype patterned media is composed of either cylindrical or truncated conical particles, so we must apply numerical methods to solve the governing equation. Since we are dealing with particles having relatively regular shapes (cylinders and truncated cones), a finite difference method (FDM) is mostly used for our study. A detailed formulation and calculation scheme will be given below. The finite element method (FEM) is an alternative method that can be used, and it is more suitable for irregularly shaped bodies since, by using tetrahedral elements, it approximates arbitrary geometries more realistically. However, it usually takes a lot of time to prepare a mesh for the computation, and, in terms of speed, there are no advantages for this method, so FDM is used instead.

2.3.1 Finite Difference Method: Discrete Formulation

Patterned media is composed of a periodic array of identical particles, so the building block of patterned media is one isolated particle. It is computationally too intensive to deal with an array of particles, so typically we analyze only one isolated particle in our micomagnetics study. For the behavior of arrays, an Ising-like interaction model is used, where we treat particles as dipoles or uniformly magnetized prisms, and evaluate their interactions. In the FDM model, a ferromagnetic particle of nickel or cobalt is represented by a three-dimensional array of cubic-shaped elements, as shown in Figure 2.1. Each element has a magnetization, represented by a constant vector. This method, by nature, works well with rectangular shapes, and results in step boundaries when applied to non-rectangular shapes. Geometrical parameters such as particle height and diameter are taken from exper-

imental measurements. The size of the cubic cell is set such that the edge length of the cell is much smaller than the exchange length, which is defined as $l_{ex} = \frac{\sqrt{A}}{M_s}$, typically a few nm. Particles smaller than the exchange length can be assumed to have an uniform magnetization, so it is important to keep the size of elemental cells below the exchange length. The general formulation for the magnetic energy density also needs to be modified for this cubic discretization, and the expression will be given below.

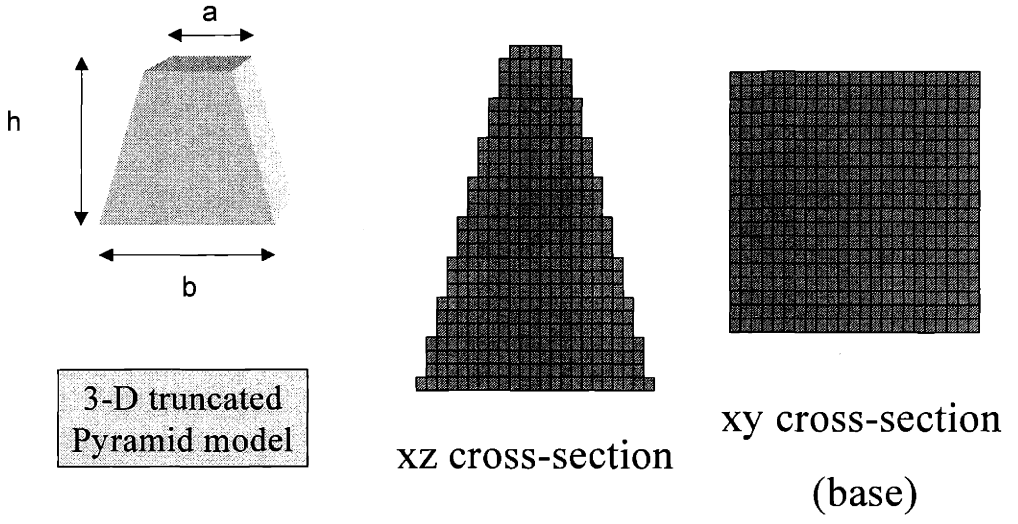

Figure 2.1: Illustration of 3D array of cubic elemental cells. *h* is the height of the particle, *b* the base diameter of the particle, and *a* the top diameter of the particle. The xz cross-section and xy cross-section of discretization is shown on the right.

2.3.1.1 Zeeman Energy

The Zeeman and the anisotropy energies are local energy densities, depending only on the magnetization of the cell under consideration. With $\vec{m}_i = \frac{\vec{M}_i}{M_s}$, the Zeeman energy per discretization element can be written as,

$$E_{app}(\vec{r}) = -\vec{H}_{ext}(\vec{r}) \bullet M_s \vec{m}_i \tag{2.16}$$

2.3.1.2 Anisotropy Energy

(1) The uniaxial anisotropy energy density per discretization element can be written as,

$$E_{an}(\hat{r}) = K_{u1}\sin^2\theta + K_{u2}\sin^4\theta \approx K_{u1}\sin^2\theta \tag{2.17}$$

The higher order terms can be neglected when K_{u1} is sufficiently large, which is the case for cobalt. This anisotropy energy density can also be written as,

$$E_{an}(\vec{r}_i) = K_{u1}[1-(\hat{k}_i \bullet \vec{m}_i)^2] \tag{2.18}$$

where $\hat{k}_i$ is the unit vector along the crystalline easy axis of the element. The latter expression is used for the actual calculation since the energy density can be computed with the magnetization vector of the cell.

(2) The cubic anisotropy energy density per discretization element is written as,

$$E_{an}(\hat{r}) = K_{c1}\left(\alpha_1^2\alpha_2^2 + \alpha_1^2\alpha_3^2 + \alpha_2^2\alpha_3^2\right) + K_{c2}\alpha_1^2\alpha_2^2\alpha_3^2 \tag{2.19}$$

2.3.1.3 Exchange Energy

Exchange energy is given as,

$$E_{ex}(\hat{r}) = \left(-\frac{2A}{a^2}\right)\left(\vec{m}_i \cdot \sum_{nn}\vec{m}_i\right) \tag{2.20}$$

where a is the center to center distance between adjacent cells, and the summation is over all nearest neighbors. The negative sign corresponds to the ferromagnetic exchange interaction induced alignment of spins along same direction.

2.3.1.4 Magnetostatic Interaction Energy

There are several ways to compute magnetostatic interaction energy. The simplest scheme is based on a dipole approximation, where each cell is equivalent to a dipole moment centered in the middle of the cell. The magnetostatic interaction energy density for each element i is then,

$$E_d(\vec{r}_i) = (M_s a^3)^2 \left(\frac{\vec{m}_i}{r_{ij}^3} \cdot \sum_j (\vec{m}_j - 3 r_{ij} (\vec{m}_j \cdot \vec{r}_{ij})) \right) \tag{2.21}$$

where a is the size of the elemental cubic cell, $\vec{r}_{ij}$ is the vector from element i to element j, and r_{ij} is the absolute value of the translation vector $\vec{r}_{ij}$.

The dipole approximation tends to overestimate the magnetostatic interaction energy for neighboring cells. Another approach to calculate the magnetostatic energy uses the gradient of a scalar magnetic potential representing the demagnetization field, and this approach is used for most of the actual computation reported here. Since we assume uniform magnetization within the elemental cubic cell, the demagnetization field can be expressed as,

$$\vec{H}_D(\vec{r}) = -M_s \vec{m}_j \int_v dv \int_{unitcell} D'_{ij}(\vec{r} - \vec{r}') dv' \tag{2.22}$$

where $D'_{ij}(\vec{r} - \vec{r}')$ is the dipole-dipole interaction kernel, written as,

$$D'_{ij}(\vec{r}-\vec{r}') = \frac{3\hat{r}_i\hat{r}_j - \delta_{ij}}{R} \quad \text{with} \quad R = |\vec{r}-\vec{r}'| \quad \text{and } i,j = 1,2,3. \tag{2.23}$$

where $\hat{r}_i = \frac{(\vec{r}_i - \vec{r}'_i)}{R}$ and $\vec{r}_i = 1, 2, 3$ is the $x,y,$ or z component of vector $\vec{r}$.

Performing the integration over the unit cell gives a demagnetization tensor, which is,

$$D_{ij}(\vec{r}-\vec{r}') = \int_{unitcell} D'_{ij}(\vec{r}-\vec{r}')dy_1 dy_2 dy_3 \tag{2.24}$$

$$= \int_{-a/2}^{a/2}\int_{-a/2}^{a/2}\int_{-a/2}^{a/2} D'_{ij}(\vec{r}-\vec{r}')dy_1 dy_2 dy_3 \tag{2.25}$$

With this demagnetization tensor, the each component of demagnetization field can be written as,

$$H_{D,i} = M_s \int_v \left(\sum_{k=1}^{3} D_{ik}(\vec{r}-\vec{r}')m_{j,k} \right) dv \tag{2.26}$$

where i = 1,2,3 and $H_{D,1}$, $H_{D,2}$ and $H_{D,3}$ represent the x, y, and z components of demagnetization field $\vec{H}_D$, respectively.

2.3.1.5 Total Effective Field

From Equation 2.7, Equation 2.8, and discrete forms of each energy term, we can obtain the total effective field for each cell,

$$\vec{H}_{eff}(\vec{r}) = -\frac{\partial}{\partial \vec{M}_i} E_{tot}(\vec{r}) \tag{2.27}$$

$$= (\vec{H}_{ext} + \vec{H}_{an} + \vec{H}_{ex} + \vec{H}_D)$$

The first term $\vec{H}_{ext}$ is a given quantity, and the second term $\vec{H}_{an}$ is the anisotropy field. For uniaxial anisotropy,

$$\vec{H}_{an}(\vec{r}) = \frac{2K_{u1}}{M_s}(\vec{k}_i \cdot \vec{m}_i)\vec{k}_i \tag{2.28}$$

For cubic anisotropy,

$$\vec{H}_{an}(\vec{r}) = -2\left(K_{c1}\alpha_1\alpha_2^2 + K_{c1}\alpha_1\alpha_3^2 + K_{c2}\alpha_1\alpha_2^2\alpha_3^2\right)k_1 \tag{2.29}$$

$$-2\left(K_{c1}\alpha_1^2\alpha_2 + K_{c1}\alpha_2\alpha_3^2 + K_{c2}\alpha_1^2\alpha_2\alpha_3^2\right)k_2$$

$$-2\left(K_{c1}\alpha_2^2\alpha_3 + K_{c1}\alpha_1^2\alpha_3 + K_{c2}\alpha_1^2\alpha_2^2\alpha_3\right)k_3$$

where k_1, k_2, and k_3 are the three crystalline axes of each cubic cell.

The third term, the exchange field $\vec{H}_{ex}$ can be written as,

$$H_{ex}(\vec{r}) = \left(\frac{2A}{M_s a^2}\right)\left(\sum_{nn}\vec{m}_i\right) \tag{2.30}$$

Note that the demagnetization field $\vec{H}_D$ was derived in Section 2.3.1.4.

2.3.2 Iterative Method: Static Calculation

The iterative method rotates the magnetization vector in each cell to the direction of the total effective field, $\vec{H}_{eff}$. This is equivalent to solving Brown's equation for static equilibrium. After sweeping through all the cells in the body, the maximum angle of this

rotation in any one of the cells is compared with a preset tolerance. This iteration continues until the maximum angle change is below the required tolerance. A well known example based on this method is a study by Schabes and Bertram on magnetic reversal in magnetic prisms [17]. The iterative method is good for small number of cells, but if the overall number of cells approaches 10,000, it becomes too slow to implement.

2.3.3 Dynamic Method

The dynamic method involves numerically solving the dynamic equation of motion, Equation 2.6. The set of 3N coupled Landau-Lifshitz-Gilbert equations is integrated until the maximum change in magnetization $(dm/dt)_{max}$ is below the preset tolerance, which is 10^{-5}. By solving the dynamic equation of motion, a transient state, which is ignored in static calculation, can be obtained, through which a reversal mechanism can be studied. Moreover, by implementing an acceleration algorithm such as Fast Fourier Transform (FFT) or Fast Multipole Method (FMM), the computation time can be reduced from $O(N^2)$ to O(NlogN) or O(N) respectively, thus enabling us to handle more complex problems. Most of our simulations employ the dynamic method rather than the iterative method.

To simulate a hysteresis loop, the magnetization of all the cells is initially aligned in the direction of the field, which is large enough to saturate the particle. The applied field is reduced by preset steps toward the reversal direction until it reaches negative saturation. For each given field, the magnetization evolves with the dynamic equation of motion until it reaches its equilibrium state. When it achieves equilibrium, the integral magnetization value is computed over the particle volume, and the field is updated. For the remanence simulation, an initial configuration is assumed; this configuration is either random, vortex or aligned in a certain direction. After saturation, the magnetization of all the cells is then

relaxed under zero field following the governing equation. The remanence value is computed upon reaching the equilibrium state. Our remanence study was first started by a collaboration with BU micromagneticians, Dr. M. Redjdal and Prof. F. Humphrey. A dynamic simulation code based on FFT is utilized for this study. Later on, a similar code was written and used for the rest of the work. Switching field studies were done through a collaboration with UCSD researchers. A general dynamic simulation code based on FMM was written by Dr. C. Seberino in Prof. Bertram's group and utilized in this study.

Chapter 3

Fabrication and Characterization

Details of sample fabrication and characterization methods are presented in this chapter. We have fabricated particle arrays of Ni and Co using Interferometric Lithography-based processes combined with electrodeposition or evaporation and lift-off, performed in the Nanostructures lab (NSL) in M.I.T. Amorphous CoP particle arrays were also made through electrodeposition. The microstructure of particles was characterized using x-ray diffraction and transmission electron microscopy. For CoP samples, the compositions of alloys were determined by energy dispersive x-ray analysis (EDX) or x-ray photoelectron spectroscopy (XPS) using Co_2P powder as a standard. After sample fabrication, hysteresis loops are measured with a vibrating sample magnetometer (VSM), a superconducting quantum interference device magnetometer (SQUID), or an alternating gradient force magnetometer (AGM). Individual nanomagnets are also characterized with magnetic force microscopy (MFM).

3.1 Fabrication Processes

We have used two sets of processes for the fabrication of arrays of nanomagnets. The process steps are illustrated in Figure 3.1. Overall, a template of holes is prepared in a trilayer resist stack, consisting of 400nm polymeric antireflective coating (ARC), 40nm evaporated silica etch mask, and 120 - 200nm photo-resist. Ferromagnetic material is deposited into those holes afterwards [18]. Figure 3.1 (a) shows the deposition of magnetic material into a template by electrodeposition. The silicon substrate is initially coated with an electron-beam evaporated plating base, consisting of layers of typically 5 nm Cr or Ti and 20-40nm Au. The photo-resist is exposed and developed to make a periodic array of holes. This pattern in the resist is transferred by reactive-ion etching (RIE) into the underlying

silica etch mask, and subsequently into ARC layer. After holes are defined in the resist stack, ferromagnetic material is deposited from a plating bath of a ferromagnetic electrolyte. This process can produce cylindrical shaped nanomagnets with high aspect ratio, which is defined by height/diameter of the cylinder. Moreover, ferromagnetic alloys such as Co_xP_{1-x}, Co_xNi_{1-x}, Co_xPt_{1-x} can be produced, thus electrodeposition was extensively used for this study. In an alternative process, magnetic material is evaporated into the template as shown in Figure 3.1 (b). After deposition, the template is dissolved, and excess magnetic material on top of the template is removed via lift-off. This process results in truncated conical structures with an aspect ratio less than 1.3. The details of each process step will be given in the following sections.

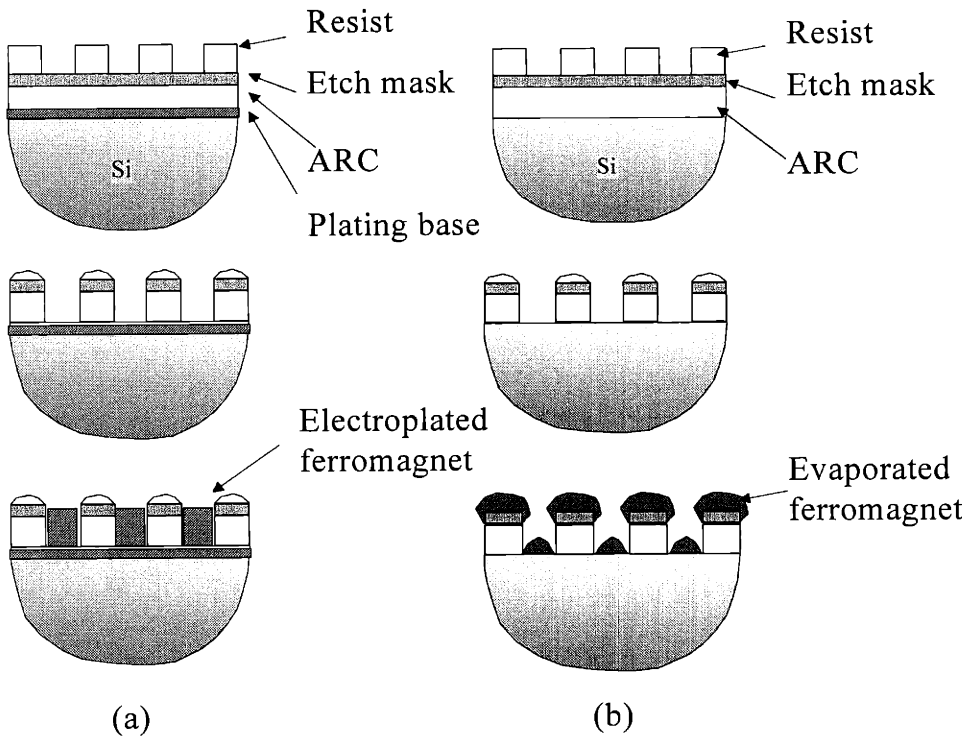

Figure 3.1: Fabrication processes employed for manufacturing arrays of nanomagnets, This figure is due to Dr. M. Farhoud (a) By electrodeposition: the substrate is first coated with a conductive plating base. After defining holes in the resist stack, ferromagnetic material is electrodeposited within the holes. (b) By evaporation and lift-off: after defining holes in the resist stack, ferromagnetic material is evaporated, then the resist stack is dissolved.

3.2 Interferometric Lithography

For early work on patterned media, electron-beam lithography was commonly employed. Electron-beam lithography provides good resolution and capability of defining arbitrary geometries, but the serial writing process is too slow to make large number of samples. Moreover, the number of nanomagnets that can be defined is limited to 10^3 or 10^4 at most, so common magnetometry techniques are difficult to use due to the small magnetic signal from the fabricated sample. To overcome these limitations, interferometric lithography

(IL) is used to make large area arrays of nanomagnets within a reasonable time.

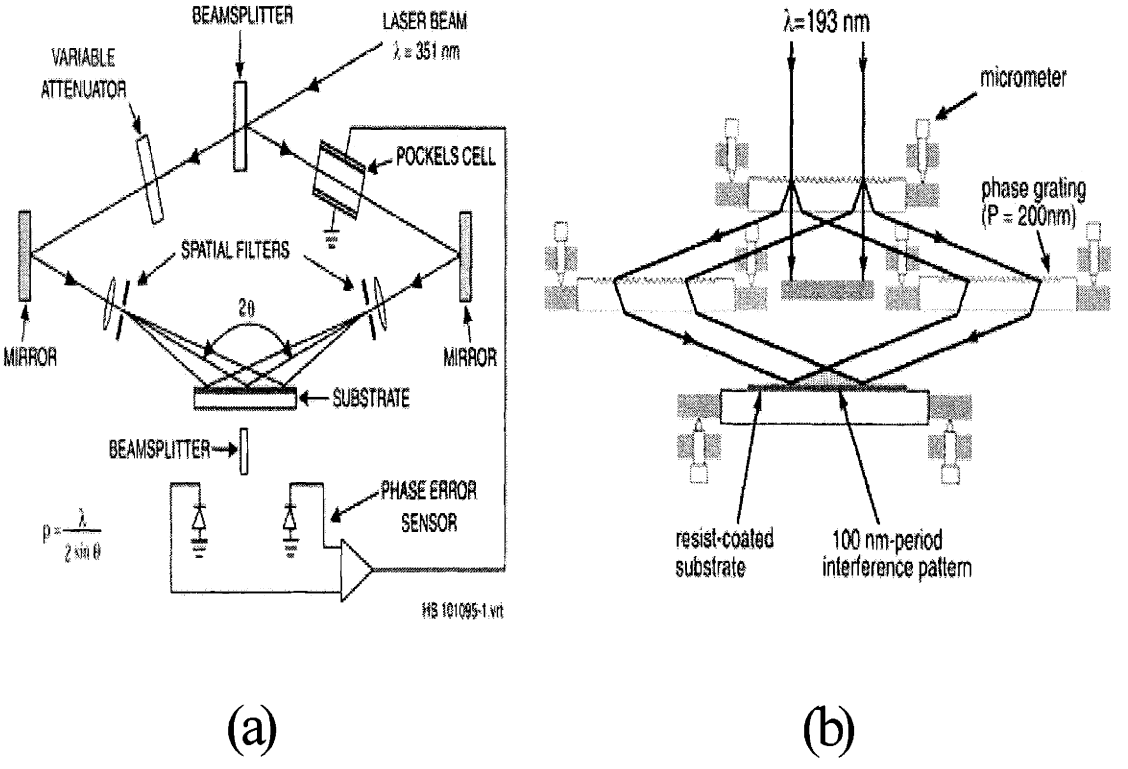

Figure 3.2: (a) Schematic of the interferometric lithography system, 351.1 nm argon ion laser beam is used.This figure is due to Dr. Mark Schattenburg (b) Schematic of achromatic interferometric lithography system developed by T. Savas. A 193 nm wavelength laser beam is used. The period of the pattern is given by exactly half of the period of the phase gratings, independent of the laser wavelength [19]

IL is based on the interference of two laser beams of wavelength λ, which intersect at an angle 2θ, on a resist-coated substrate. A sinusoidal standing wave pattern is formed at the substrate with a period given by $\lambda/(2\sin\theta)$. A second exposure after rotating the substrate 90° generates a grid pattern, which can be used to define a set of holes in the resist stack. 200nm period structures are made by IL, and 100nm period structures are made by achromatic interferometric lithography (AIL). For AIL, a polymethyl-methacrylate (PMMA) positive resist is used. For IL, a negative I-line resist, THMR-iN PS1 made

by OHKA, America is used since a negative resist process is much better suited for making hole patterns due to an increase in contrast and process latitude [18,20,21]. By changing exposure dose and development time, the size of holes is controlled. The hole diameter decreases with increasing exposure dose, and 10 - 15 mJ/cm^2 is used for the template fabrication [22]. Figure 3.2 shows schematics of MIT's IL systems: Conventional interferometric lithography system developed by Dr. Mark Schattenburg and achromatic interferometric lithography system developed by Dr. Tim Savas.

3.3 Pattern Transfer and Structural Characterization

After holes are defined in the photo-resist by IL, the pattern is transferred into the silica etch mask by reactive ion etching in a CHF_3 plasma at a 300 V DC bias. Subsequently, the ARC is etched in an O_2 plasma. All template preparation steps were done by Dr. Maya Farhoud at the NSL. The holes formed in photo-resist by IL and transferred into the ARC layer are shown in Figure 3.3. Using this template as a mold, nanomagnets are defined by either electrodeposition or evaporation/lift-off. After the fabrication, scanning electron microscopy (SEM) is done to identify particle shapes and to measure the height and diameter of the particle. All SEM work was done in the NSL using a Zeiss/Leo Gemini 982. $\theta - 2\theta$ x-ray diffraction is used to check the grain size and texture of samples. A Rigaku Rotaflex RU 300 system in the Center for Materials Science and Engineering (CMSE) at MIT was used for these experiments. High voltage transmission-electron microscopy (TEM) was also used to confirm the microstructures of particles. The particles of interest were scraped onto a carbon grid. The particles were electron-transparent at 400 kV, so could be imaged without thinning. All TEM work reported in this thesis was done by Dr. F. M. Ross at IBM, Yorktown Heights. For CoP samples, compositions of alloys were determined by energy dispersive x-ray analysis (EDX) or x-ray photoelectron spectroscopy (XPS) using Co_2P powder as a standard.

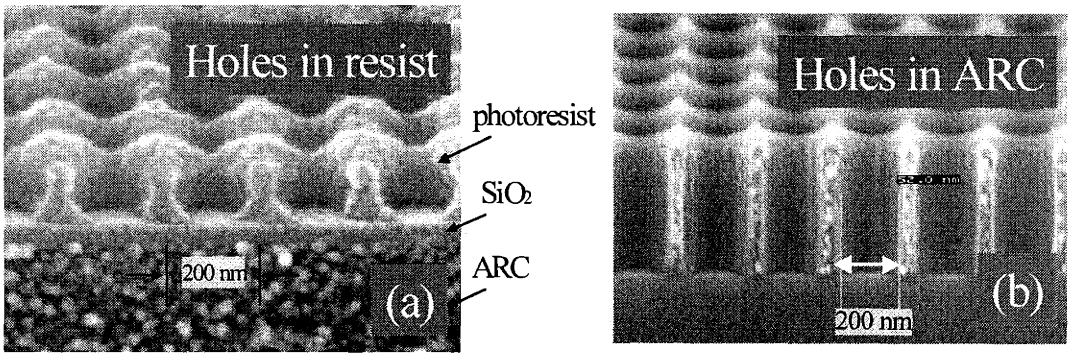

Figure 3.3: Scanning electron micrographs of template preparation steps. This figure is due to Dr. Maya Farhoud (a) Holes are formed in photoresist by IL. (b) The holes are transferred into the ARC layer by etching.

3.3.1 Electrodeposition

To obtain high shape anisotropy, the aspect ratio of the nanomagnets should be high. The popular lift-off process cannot be used for high aspect ratio vertical structures. In the lift-off process, gradual accumulation of materials at the orifice of each template opening during the deposition will eventually close the opening; as a result, the maximum nanomagnet height is about the size of the template opening and large shape anisotropy is difficult to achieve. Electrodeposition is an attractive method for filling such high aspect ratio holes economically and effectively, thus it was used extensively in this study to form Ni, Co, CoP cylinder arrays with aspect ratios ranging from 0.7 to 3. Prior to electrodeposition, the substrates were rinsed with distilled water. The cathode of a DC power supply is connected to the plating base of the substrate using an alligator clip, and the anode of the power supply is connected to platinum-coated niobium mesh. Subsequently the substrate and the anode are immersed in the plating bath. All depositions were carried out in a well-agitated bath on a hot plate. The height of the nanomagnets was controlled by varying the deposition time. Constant current is used instead of constant potential due to a better con-

trol of the height. The microstructure and the following magnetic properties of the deposited metal films can be controlled by deposition conditions such as electrolyte composition, temperature, current density, pH value, and agitation rate. The details of deposition of each ferromagnetic material are given below and summarized in Table 3.1.

Metal	Electrolyte	Contents	pH	Temp	Current density (mA/cm^2)
Ni	Ni-sulfamate	$Ni(SO_3NH_2)_2$ (1.3 M) H_3BO_3 (0.7 M)	3.5	50	1 - 11
Co	Co-sulfate	$CoSO_4$ (1.5 M) H_3BO_3 (0.5 M)	3.5	25	4 - 8
	Co-sulfamate	$Co(SO_3NH_2)_2$ (1.3 M) H_3BO_3 (0.7 M)	3.5	25	4 - 8
CoP	CoP-A	$CoCO_3$ (0.1 M) $CoCl_2$ (0.7 M) H_3PO_3 (0.5 M)	1.6	60	10 - 1000
	CoP-B	$CoSO_4$ (1.0 M) $CoCl_2$ (0.2 M) H_3PO_3 (12 - 120 mM) H_3BO_3 (0.5 M)	1.6	60	10 - 1000

Table 3.1: Electrodeposition condition summary (partially due to Dr. M. Shima)

The resulting structure after electrodeposition is shown in Figure 3.4. The cylindrical particles have straight sides, with a slight taper in some cases due to an increase in the hole diameter through the thickness of the ARC. Larger-diameter particles often showed concave top surfaces, due to current crowding at the edges, but as the particle height approached the template thickness the top surfaces tend to become convex as shown in Figure 3.4 (c). After deposition, the ARC template could be removed using oxygen RIE to obtain better images of particles by SEM.

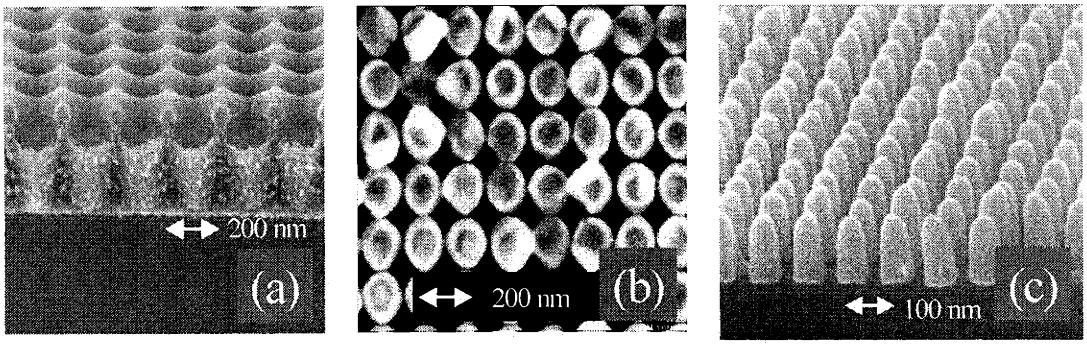

Figure 3.4: Scanning electron micrographs of electrodeposited structures. (a) Cross-sectional view of an array of electrodeposited Ni still embedded in ARC (b) Top view of electrodeposited Co (c) Cross-sectional view of an array of electrodeposited Ni after removal of ARC. (Figure (c) is due to T. Savas)

3.3.1.1 Electrodeposition of Nickel

Nickel was deposited from a commercially available sulfamate electrolyte (Barrett SN sulfamate nickel) from MacDermid. Barrett SN contains 327 g/L of anhydrous nickel sulfamate (equivalent to 76.5 g/L of Ni metal), 30 g/L of boric acid, 3 g/L of a proprietary anode corrosion aid and 0.3% by volume of wetting agent. Manufacturer specifications show that at a bath temperature of $54°C$, the stress of the film is equal to zero. To operate the bath at $50°C$, boric acid content was increased to 45 g/L to adjust the pH to 3.65. All deposition is carried out in a well-agitated bath on a hot plate. Galvanostatic plating is done where the current between the anode and cathode is kept constant. Current densities are varied from 1 to 11 mA/cm^2. According to Krauss. et. al., for their nickel plating, the optimum stirring speed for micron scale features was found to be between 100 and 125 rpm [23]. Stirring speeds lower than this resulted in only shallow filling of the template features and speed higher than this resulted in rough film surfaces [23]. So, the bath is well agitated with a magnetic stirring bar rotating at 125 rpm. X-ray diffraction analysis of both patterned and unpatterned samples indicates that the deposits are polycrystalline with a

grain size of approximately 10nm and a weak (111) f.c.c. preferred orientation. TEM observations show that as-deposited Ni was polycrystalline with a grain size of 10 - 20nm. (Figure 3.5) However, annealing the smaller particles during the ARC template removal process could result in recrystallization, and the final microstructure then consisted of single-crystal particles with occasional grain boundaries or stacking faults as shown in Figure 3.5. (b). The annealing process also created a thin oxide layer of ~5nm on the surface of the particles, and causes some rounding of the top surface.

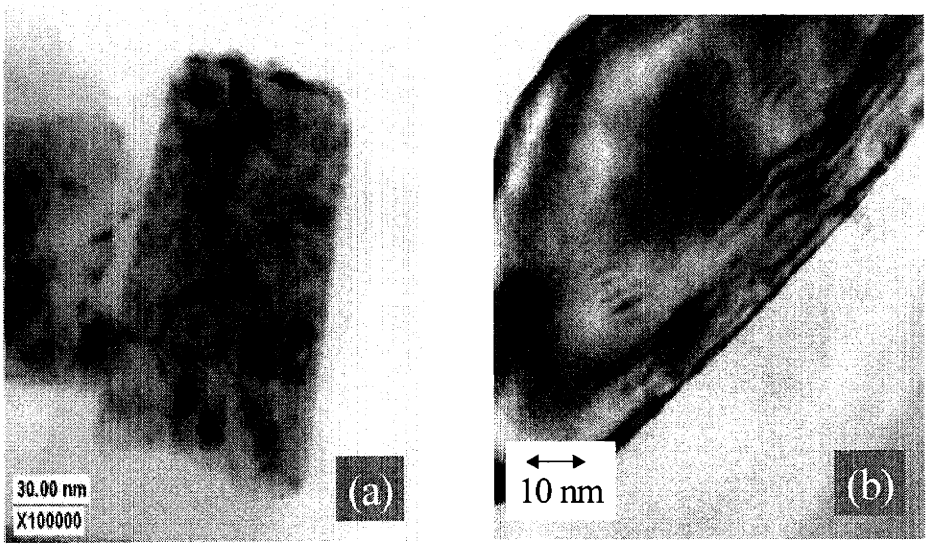

Figure 3.5: Transmission electron micrographs of an electrodeposited Ni pillar (shown up-side-down) (a) As-deposited Ni is polycrystalline with a grain size of 10 - 20nm. (b) Annealed Ni is a single crystal with a thin oxide layer of ~5nm on the surface. Figures are due to Dr. F. Ross

3.3.1.2 Electrodeposition of Cobalt

Cobalt was initially deposited from a sulfate electrolyte. The sulfate solution contained 230 g/L cobalt sulfate and 30 g/L boric acid with pH of 3.5. A sulfamate solution was also used. The sulfamate solution was a commercial electrolyte from McDermid containing 75 g/L cobalt metal and 45 g/L boric acid, and the pH is adjusted by addition of cobalt car-

bonate or sulfamic acid in the range of 3.5 to 4.0 For both cases, the deposition was mostly carried at room temperature, since lower temperature deposition results in finer size grains and the c-axis (magnetic easy axis) out-of-plane. The grain size of the resulting films is also affected by the pH of the bath. pH 3.5 - 4.0 yields the finest size grains with mean roughness of 5nm, confirmed by Atomic force microscopy (AFM), so this value was used for most of the depositions. For tall nanomagnets, we had a problem of large crystal growth, thought to come from the preferred growth of some Co grains. This large crystal growth is shown in Figure 3.6. This problem can be solved by using a thicker ARC template, or grain refiners. X-ray diffraction results show that Co samples deposited from both a sulfate and a sulfamate electrolyte were polycrystalline with a grain size of 10 - 20nm and a weak (0002) h.c.p. preferred orientation, which improved with increasing current density.

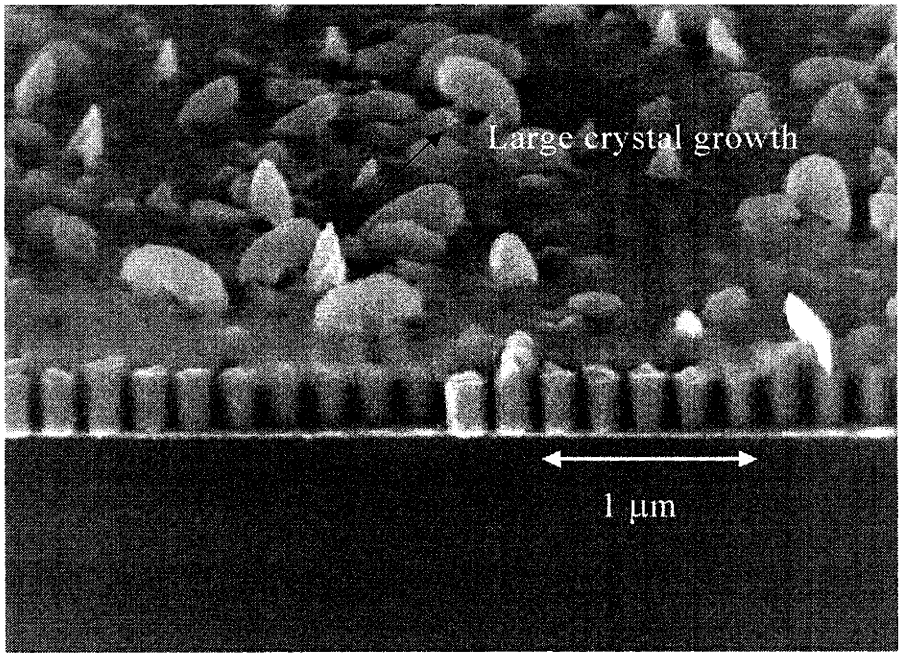

Figure 3.6: Large crystal growth due to the preferred growth of some Co grains in electrodeposited Co nanomagnets

3.3.1.3 Electrodeposition of Cobalt Phosphorus

Electrodeposition of CoP is considered to be induced codeposition since phosphorus cannot deposit alone from aqueous solution [24]. We intended to remove magnetocrystalline anisotropy by making amorphous films to see the effect of shape only on the magnetic properties. Moreover, by making alloys, we can tune the saturation moment, and investigate the change of magnetic properties with this change in the saturation moment. Thus, CoP is chosen, since it is known to form an amorphous film over a wide range of phosphorus content [25, 26]. This study is conducted together with Dr. M. Shima in our group. The template was masked with an electroplating tape to define the deposition area of about 1 cm^2 to obtain a high current density such as 10 - 1000 mA/cm^2 with a 1 - 2A current source. Both patterned and unpatterned CoP films were studied. Our XPS results show that the phosphorus content in the CoP films decreases as the current density increases and the higher the H_3PO_3 content in the electrolyte, the higher the phosphorus content in the CoP films [27]. X-ray diffraction showed that the alloy is polycrystalline for low P content, but is amorphous when the phosphorus content is greater than 15 at %. The saturation magnetization, M_S and coercivity, H_c measured for the samples are plotted as a function of phosphorus content, X, in the $Co_{100-x}P_x$ films. (Figure 3.7) The saturation magnetization from the samples made from the electrolyte with 24 mM H_3PO_3 decreases linearly as X increases. The M_S value for the samples from the bath with 120 mM H_3PO_3 drops at X ~ 15 % where the structure of the films changes from polycrystalline to amorphous. The coercivity for samples from both electrolytes also drops rapidly from ~ 30 Oe to around 1-2 Oe at X ~ 15%. For patterned sample fabrication, a current density of 150 mA/cm^2 and an electrolyte containing 120 mM H_3PO_3 were chosen, in order to obtain an amorphous CoP cylindrical particle array with phosphorus content of 22 %, where the expected value of M_S is 300 - 500 emu/cm^3.

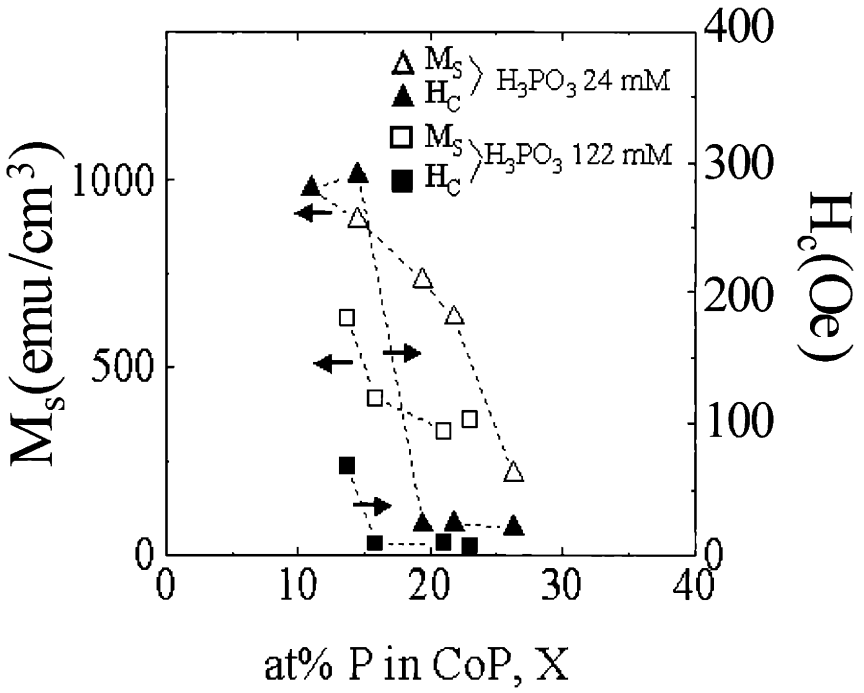

Figure 3.7: Saturation moment and coercivity as a function of the phosphorus content X in electrodeposited $Co_{1-x}P_x$ alloy films. The composition values were measured using EDX and calibrated by the value for standard Co_2P powder [27]

3.3.2 Evaporation/ Lift-off

In an alternative process, the ferromagnetic materials can be deposited into the template by evaporation. The evaporation of material into a template produces truncated conical shapes with an aspect-ratio (height-to-base diameter ratio) less than about 1.5 or 2. All evaporation sample fabrication was done by Dr. M. Farhoud and J. Daley in the NSL. Ni and Co were electron-beam evaporated into the template of holes at a base pressure of approximately $5 \cdot 10^{-6}$ Torr and a deposition rate of 0.5 nm/s. The evaporation template

and excess material on top is removed in a H_2O:H_2O_2:NH_4OH solution. The resulting structures are demonstrated in Figure.3.8. X-ray diffraction shows that the evaporated films are polycrystalline. Ni films have a preferred f.c.c. (111) texture, while cobalt films show strong preferred h.c.p. (0002) texture. The angular distribution of c-axes in the Co was assessed from the (0002) rocking curve, which had a half-width of $13°$. Thus the majority of the c-axes are distributed within a cone of semi-angle $6.5°$ with axis normal to the film plane. Transmission electron micrographs of evaporated Ni particles were obtained in the same way as for electrodeposited particles (Figure 3.9). Nickel particles are surrounded by a thin native oxide layer with a thickness of 3 - 4nm. The particles have a columnar grain structure with the grains often extending through the film thickness, and grain diameters of 10 - 20nm. Evaporated Co particles are expected to have a similar columnar microstructure.

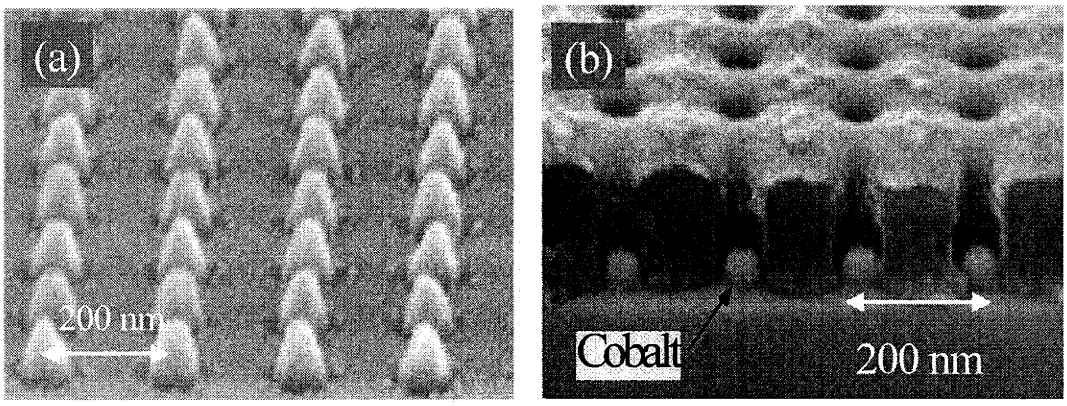

Figure 3.8: Scanning electron micrographs of evaporated structures. (a) An array of evaporated Ni after removal of ARC (b) Cross-sectional view of evaporated Co still embedded in ARC (Figures are due to Dr. M. Farhoud)

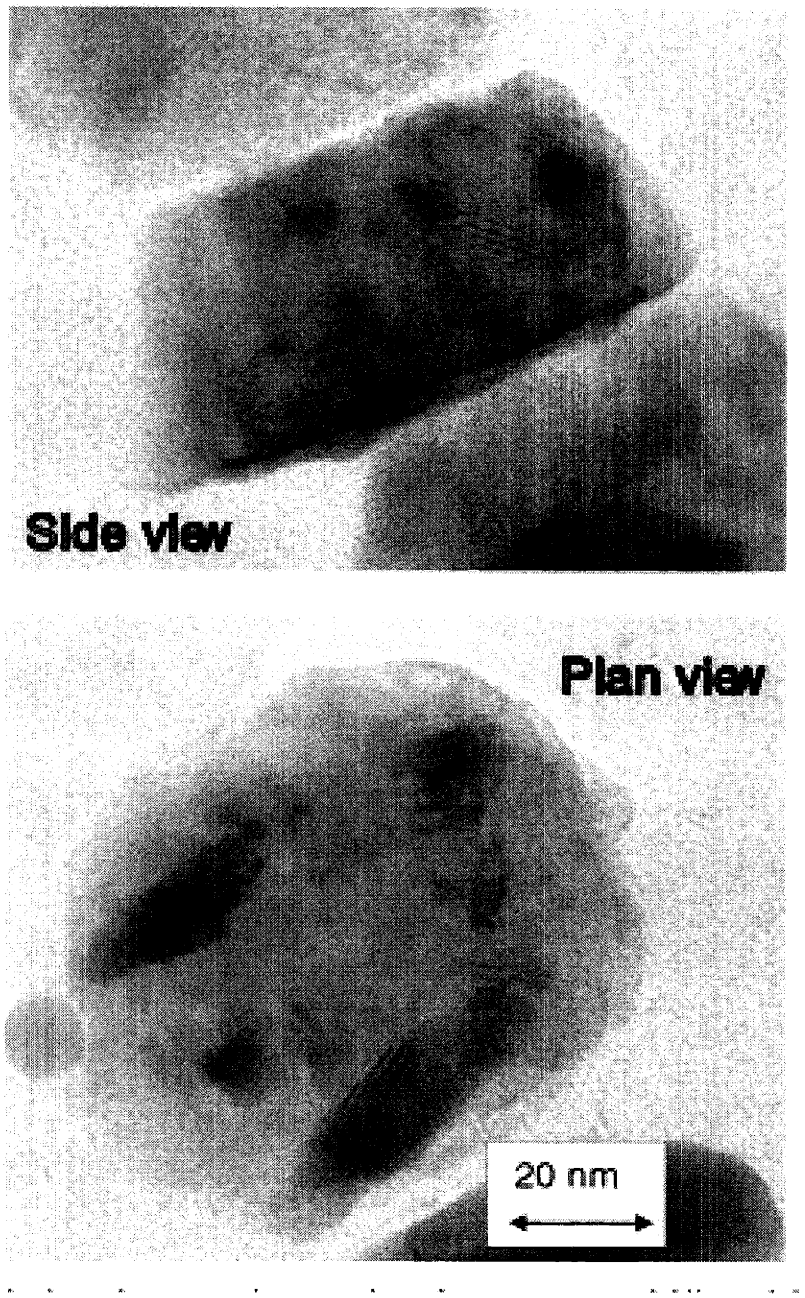

Figure 3.9: Transmission electron micrograph of an evaporated Ni particle (a) a cross-sectional view. (b) A top view. (due to Dr. F. Ross)

3.4 Magnetic Characterization

3.4.1 Bulk Characterization: Magnetometry

Bulk magnetic characterization was carried out using a vibrating sample magnetometer (VSM), a superconducting quantum interference device (SQUID) magnetometer, and an alternating gradient force magnetometer (AGM). Major hysteresis loops at room temperature were measured for all the samples, which gives the collective magnetic behaviors of the particle arrays. A hysteresis loop gives a variety of technical parameters for magnetic materials such as saturation moment, coercivity, remanence, magnetic anisotropy, and insight into switching mechanism of particles. Initially, a DMS/ADE 1660 VSM was used for most measurements. The sensitivity of the machine is about 10^{-5} emu, and the measurements usually took about 40 minutes depending on the number of averages taken for each data point. Later on, our laboratory acquired an AGM. Because of improved sensitivity (~10^{-7} emu) and shortened measurement time (~2 min), AGM was generally used for all subsequent samples. For a selected few samples, low temperature hysteresis loop measurements were performed with a SQUID magnetometer to gain more insight on switching characteristics. Although the sensitivity of a SQUID magnetometer is comparable to that of AGM, sample mounting in a SQUID magnetometer is somewhat more difficult and the data acquisition time (~5 hours per loop) is much longer. Thus, a SQUID magnetometer was used only for low temperature measurements. The operating principle of each magnetometer can be found in [28,29,30].

3.4.2 Imaging Individual Nanomagnets: Magnetic Force Microscopy (MFM)

MFM measurement were made using phase contrast imaging with a vibrating cantilever (Digital Instruments Dimension 3000 SPM). Most of the MFM images were taken by Dr. M. Farhoud at NSL and M. C. Abraham at Prof. R. J. Ram's lab. The magnetic cantilever's resonant-frequency shifts as a result of tip-sample interactions. This results in a phase shift in the cantilever oscillation at resonant frequency given by [31]:

$$\Delta\phi = \frac{Q}{k}(\vec{m} \cdot \nabla^2 \vec{H}) \tag{3.1}$$

where $\Delta\phi$ is the phase change of the cantilever oscillation, Q the quality factor, k the spring constant, and $\vec{m}$ the magnetization of the cantilever. The magnetization of the tip is directed perpendicular to the plane of the sample being imaged. Thus, regions in the sample having magnetization components out of the plane of the sample produced regions of bright contrast and vice-versa. Accordingly, an out-of-plane magnetized single-domain particle will be shown as either a black or a white dot. Moreover, a switching event can be detected by the change of the color either from black to white or from white to black with an externally applied field. For some particle arrays, the switching field distribution was measured and compared with VSM measurements and theoretical predictions. The commercial tips used were made of etched silicon with a tip radius of approximately 30nm and a sputtered 40nm layer of CoCr (this is a regular moment tip). For non-destructive imaging of the demagnetized state of a sample, lower moment tips, which are sputtered with 15 nm of the same CoCr alloy, are used instead. Representative MFM pictures showing single-domain particles are given in Figure 3.10.

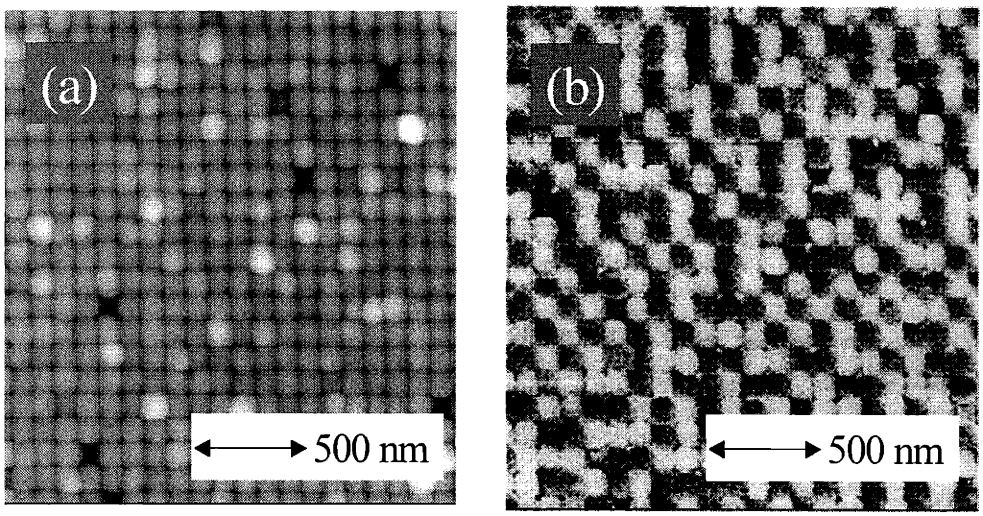

Figure 3.10: Two corresponding micrographs of the topography and phase image of electrodeposited Ni sample (58 nm in diameter, 115nm high, period: 100nm), acquired by magnetic force microscopy. (a) Topography (b) phase image, which indicates the second partial derivative in z of the z-component of the H field above the sample. White dot means tip-sample repulsion, and black dot means attraction.(Picture is taken with the support of M. C. Abraham)

Chapter 4

Evaporated Conical Samples

In this chapter, experimental results on evaporated conical particles are compared with micromagnetic simulations results. In particular, the influence of size, aspect ratio, and anisotropy on the remanent states of nanomagnets is investigated. A large number of Ni and Co samples were fabricated by evaporation/lift-off process. All samples have a period of 200nm. Table 4.1 summarizes the dimensions and magnetic properties of the particles used in this study. These particles can be described as truncated circular cones with height h, base diameter b, and top diameter a. Aspect ratio R is defined as the ratio of the particle height-to-base diameter. The nearest neighbor interaction field is computed and compiled in the table, assuming the particle behaves as a dipole. For parallel dipoles side by side, the nearest interaction field $H_i = M_s V/p^3$, where M_s is the saturation moment, V is the particle volume, and p is the spacing of the particles, equal to the period of the array. For parallel dipoles arranged end-to-end, $H_i = 2M_s V/p^3$. Since the interaction field is quite small, these particle arrays can be described as 'weakly interacting', i.e. the collective magnetic behavior is mostly governed by the behavior of single isolated particle. Figure 4.1 shows scanning electron micrographs of the nickel samples and their room temperature hysteresis loops measured parallel and perpendicular to the substrate by VSM, in order of increasing aspect ratio. Figure 4.2 shows similar sets of data for the cobalt samples.

4.1 Experimental Observation

For both Ni and Co, a change in net anisotropy occurs for aspect ratio $R = 0.65$. For particles with $R > 0.65$, the out-of-plane direction is an easy axis with coercivity of up to 600 Oe for the tallest particles (R = 1.2), while the in-plane direction is a hard axis. For

flat particles, with $R < 0.65$, the in-plane direction is a easy axis. This is unexpected since ideal-shaped bodies such as ellipsoid or prisms are known to have this transition at an aspect ratio $R = 1$, unless there exists an strong anisotropy due to the crystal structure favoring an alignment along a certain direction. Moreover, for the samples with $R > 0.65$, MFM indicates dipolar magnetization states with high axial (out-of-plane) remanence. A close look at in-plane measurements reveals another interesting point. Since these particles have a circular symmetry, free rotation of magnetic spins in the plane would result in zero in-plane coercivity. However, in-plane coercivities of 30 - 70 Oe for Ni and 90 - 220 Oe for Co are observed, indicating pinning of the magnetization, presumably due to edge irregularities, grain boundaries, or other microstructural features [32]. Since Co has a larger uniaxial anisotropy compared to Ni, which has a weak cubic anisotropy, it seems plausible to observe higher in-plane coercivity for Co. Since it is hard to separate the effect of microstructure from shape effects (size, aspect ratio, and geometry) in experiments, micromagnetic simulations are performed to give insight about the understanding of experimental results. The details of this simulation study is given in the following section.

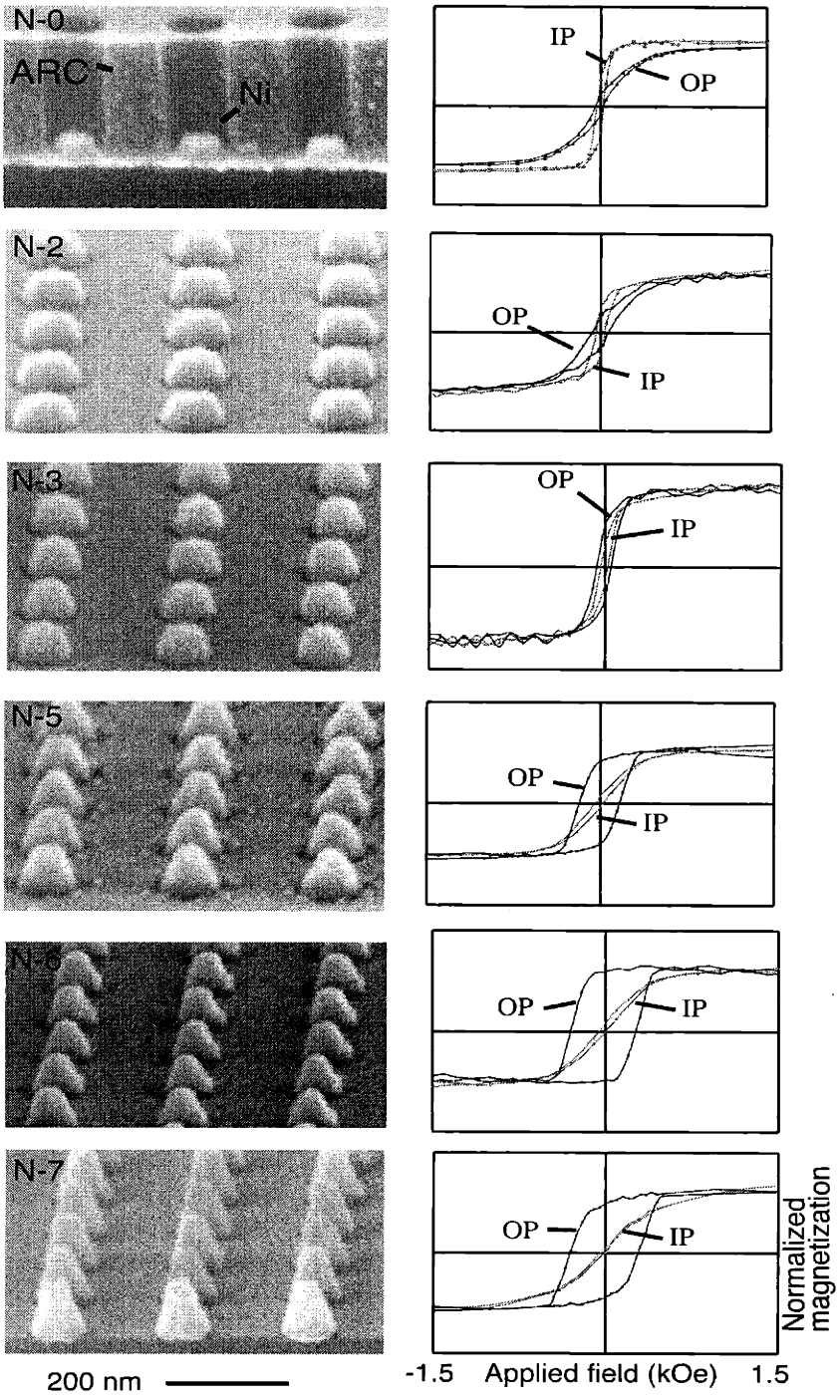

Figure 4.1: Scanning electron micrographs and corresponding hysteresis loops of evaporated Ni samples. This figure is due to Dr. M. Farhoud

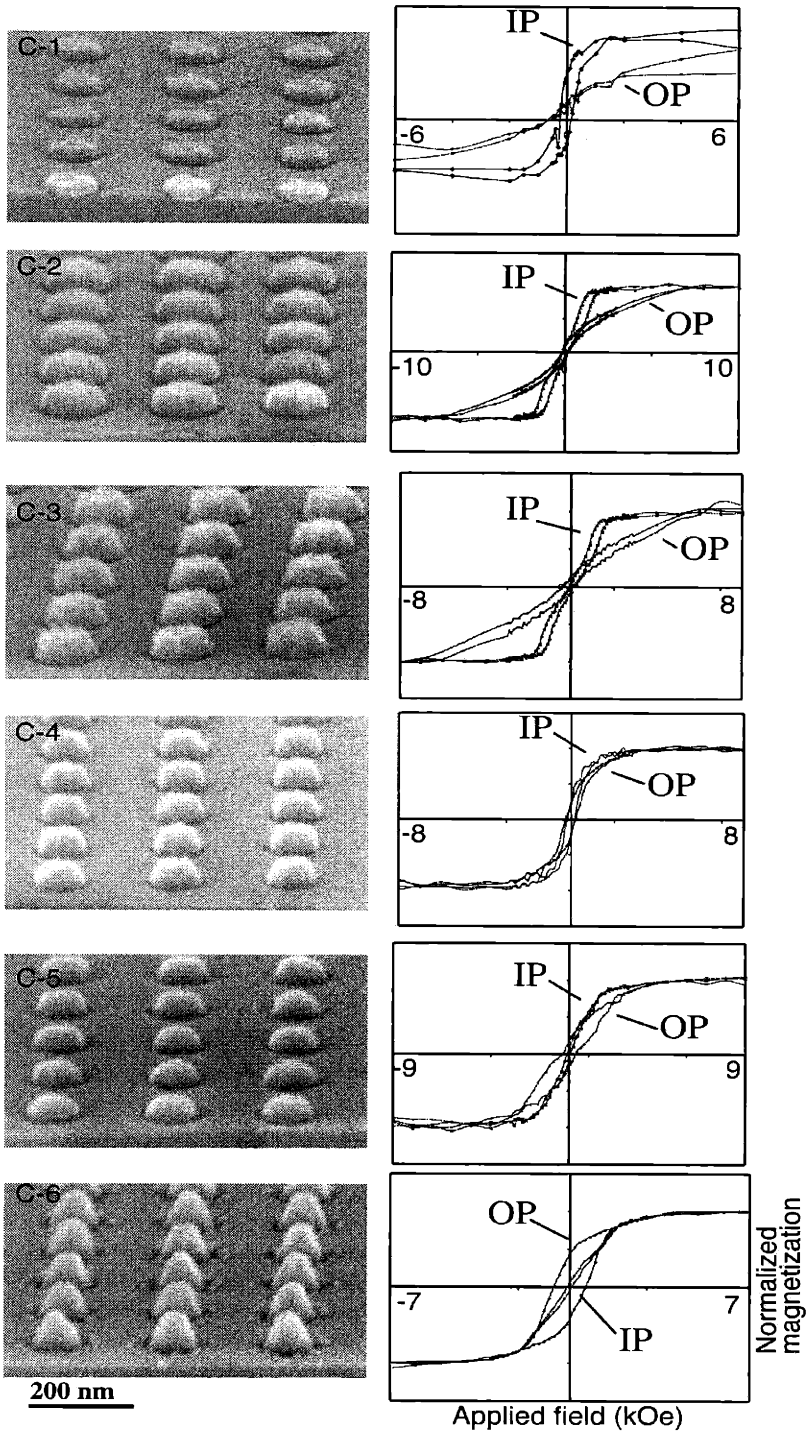

Figure 4.2: Scanning electron micrographs and corresponding hysteresis loops of evaporated Co particles. This figure is due to Dr. M. Farhoud

Sample	Height h (nm)	Base b (nm)	Top a (nm)	Aspect ratio R = h/b	Coercivity in plane (Oe)	Coercivity out of plane (Oe)	Nearest neighbor field H_i (Oe)
N-0	35	80	57	0.43	60	60	8
N-1	55	122	107	0.45	42	179	34
N-2	55	89	50	0.62	77	145	13
N-3	55	84	60	0.65	59	118	14
N-4	55	75	45	0.73	32	201	10
N-5	80	89	36	0.90	69	347	16
N-6	80	80	36	1.00	61	560	13
N-7	110	91	37	1.21	35	586	23
C-1	20	95	76	0.22	220	100	20
C-2	55	125	90	0.44	162	136	89
C-3	55	123	85	0.45	130	227	84
C-4	55	86	85	0.64	168	223	56
C-5	55	79	50	0.70	91	340	32
C-6	80	85	32	0.94	87	620	41

Table 4.1: Dimensions and magnetic data for evaporated samples, with nearest neighbor interaction fields calculated assuming that the particles are saturated.

4.2 Remanent State Studies by Micromagnetics

4.2.1 Modeling Details

Particles are modeled as truncated cones, or pyramids by stacking up either circles or squares made from cubic elements. The particle is represented by $N_x \times N_y$ cubic elements in the xy plane for the base of the particle. Along z, perpendicular to the base, N_z elements represent the height. The volume of the particle was divided into between 6000 and 16000 elements, with N_x=N_y=23 or 31, and N_z = 12 - 35 depending on the desired aspect ratio. The angle between the sidewalls and the base plane was fixed at $72°$. Length scales are normalized with respect to the exchange length $l_{ex} = \sqrt{A}/M_s$, where A is

the exchange constant and M_s the saturation magnetization [33]. The size of the cubic elements was kept below 0.5 l_{ex} even for the largest size particles to ensure robust computations. Even though the surfaces are represented by discrete steps due to the cubic mesh, with the discretization size equal to 1/31 or 1/23 of the particle diameter, the surface roughness was smaller than l_{ex} for all the particle sizes modeled. Thus, the surface roughness is not expected to introduce significant error into the calculation [34]. Since initial calculations on truncated cones showed similar results to truncated square-based pyramids, only results on truncated pyramids are presented. An exchange constant of $A = 10^{-6}$ erg/cm was used for both Co and Ni particles. Saturation magnetizations M_s of 484.1 and 1420 emu/cm^3 were taken for Ni and Co, respectively, so the exchange length was 20 nm for Ni and 7 nm for Co. A uniaxial magnetocrystalline anisotropy K_u from zero to 3.0x10^6 erg/cm^3 parallel to the particle axis was included. A Single-crystal Ni particle with the [111] crystal axis aligned with the axis of the particle would have magnetocrystalline anisotropy of 5x10^4 erg/cm^3. This sets the maximum magnetocrystalline anisotropy value we can expect from polycrystalline Ni particles, so the change of remanent state with the inclusion of this anisotropy along the particle axis is studied. Moreover, the columnar grain structure of Ni particles can result in another anisotropy, which is determined to be order of 2x10^5 erg/cm^3 from a previous study, so this value is also used for the numerical study. Finally, from the x-ray study on evaporated Co, we know that preferential alignment of the c-axes perpendicular to the film would result in strong anisotropy along the particle axis. The magnitude of this anisotropy can be estimated from the distribution of *c*-axes determined by the x-ray diffraction rocking curve for a blanket film. From integrating the contributions from each grain, we obtained a net out-of-plane anisotropy of $0.66K_u$, where K_u=4.5x10^{6}erg/cm^3 is the uniaxial anisotropy of Co.

4.2.2 Effect of Particle Size on Remanence

First the effect of particle size on remanence is considered. In Figure.4.3, axial remanence is shown as a function of normalized diameter b/l_{ex} for three cases, (a) an aspect ratio of $R = 1.13$ and $a/b = 0.35$ with zero anisotropy, (b) a taller and sharper particle with $R = 1.22$ and $a/b = 0.22$ with zero anisotropy, and (c) the same geometry as (a) but with an anisotropy field, defined as $2K_u/M_s$, of 4191 Oe, corresponding to $0.66K_u$ of pure Co. This particular value was chosen for comparison with experimental results. For tall particles with $R > 0.9$, the squareness S, which is defined as axial remanence divided by saturation moment, is almost constant at 1.0 until the diameter b reaches a critical value above which S begins to decrease. For the zero anisotropy case, shown in Figure.4.3, the critical diameter is $3l_{ex}$. Below this diameter, an "out-of-plane flower" state exists where the squareness is very close to 1 and the magnetization is almost parallel to the axis except for small deviations at the corners. Above the critical diameter, a helical vortex develops along the central axis of the particle and magnetization vectors become tilted into the sample plane. This helical vortex develops first near the base of the particle, and extends through the particle as the particle size increases, leading to a gradual decrease in S. Even larger particles ($b > \sim 10l_{ex}$) show multi-domain states, and the axial remanence is close to zero. The addition of uniaxial anisotropy parallel to the axis of the particle, as in Fig.4.3(c), makes the flower-to-vortex transition occur at larger critical diameters and increases the axial remanence of vortex states significantly. The flower-vortex transition now occurs at $5l_{ex}$, but the remanence decreases only slowly above this, and stays above 0.7 for diameters up to $10l_{ex}$, which is about the size of the Co particles we investigated.

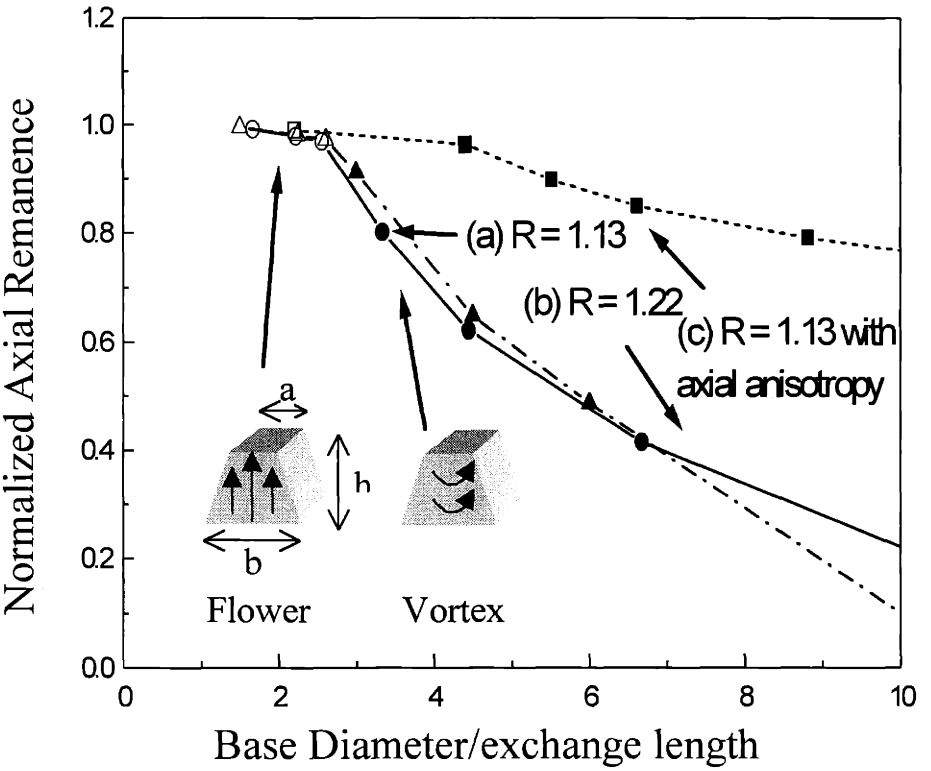

Figure 4.3: Calculated axial remanence for truncated pyramidal particles after axial saturation, as a function of normalized base diameter. (a) Aspect ratio R = 1.13, a/b = 0.35, zero anisotropy; (b) R = 1.21, a/b = 0.22, zero anisotropy; (c) R = 1.13, a/b = 0.33, with axial anisotropy corresponding to 3.0×10^6 erg/cm^3 for Co particles.

In contrast, short particles ($R < 0.9$) have low axial remanence. At small diameters the particle shows an "in-plane flower" state in which the magnetization is parallel to the base plane. Larger particles develop vortex or multi-domain structures. Figure 4.4 shows the three different types of remanent states for small particles: out-of-plane flower, in-plane

flower and vortex states. Figure 4.5. shows the remanent magnetization patterns both for an xz cross-section through the particle and for the xy basal plane.

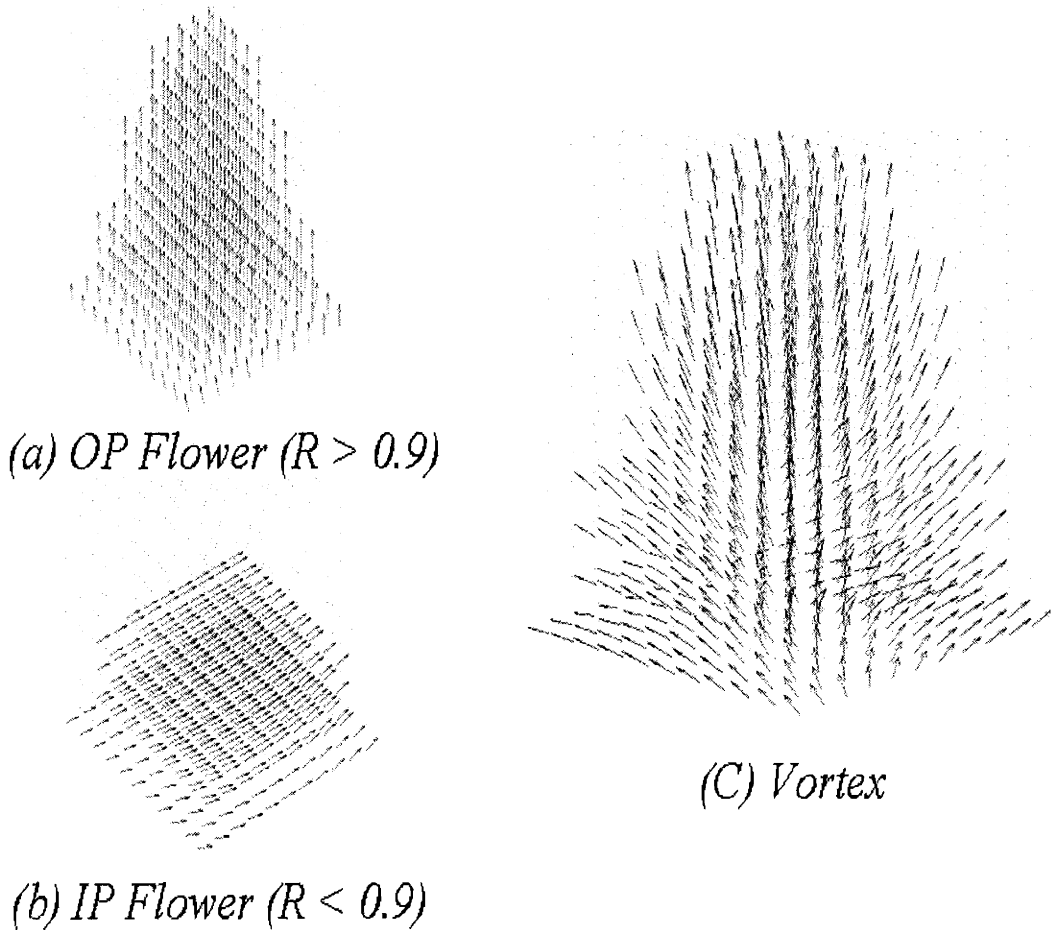

Figure 4.4: 3D magnetization vector plots of remanent states. (a) Out-of-plane flower state, $R=1.13$, $b=1.5l_{ex}$, (b) In-plane flower state, $R=0.45$, $b=2l_{ex}$, (c) Helical vortex state, $R=0.9$, $b=4l_{ex}$

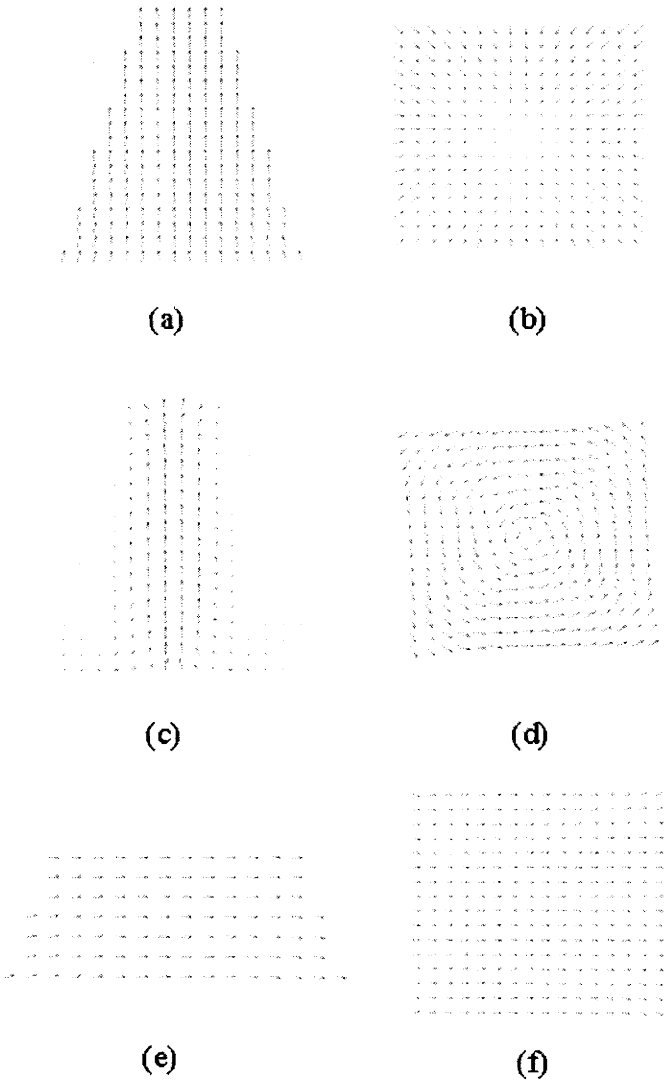

Figure 4.5: Cross-sections through particles, showing the remanent magnetization distribution. The arrows show the direction of magnetization. The arrow length is proportional to the component of the magnetization parallel to the page. For clarity, only one out of every four discretization cells is shown. (a) Base diameter $b = 1.5l_{ex}$, aspect ratio $R = 1.13$, cross-section parallel to axis, showing out-of-plane flower state. (b) Same particle as (a) showing the magnetization in the base plane. (c) $b = 10.9l_{ex}$, $R = 1.13$, cross-section parallel to axis, showing a vortex state (d) Same particle as (c) showing the magnetization in the base plane (e) $b=2l_{ex}$, $R=0.45$, cross-section parallel to axis, showing in-plane flower state. (f) Same particle as (e) showing the magnetization in the base plane.

4.2.3 Effect of Aspect Ratio on Remanence

The effects of varying the aspect ratio on the flower and vortex states were studied. For the flower states, the base diameter was fixed at $2l_{ex}$ and the height of the particle was changed. The particle shows a flower state at all aspect ratios but there is an abrupt transition from out-of-plane to in-plane flower states at R=0.9 (Figure 4.6.) This is similar to the critical aspect ratio analytically obtained for a uniformly magnetized cylinder, which is 0.9065 [35]. Adding anisotropy along the axis of the particle reduces the critical aspect ratio. Similar tests were performed for vortex-state particles.

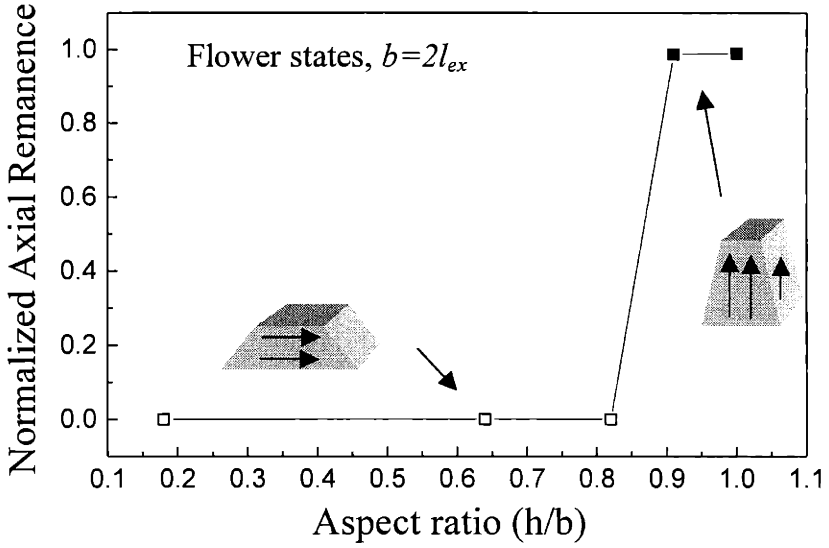

Figure 4.6: Calculated remanence along the axis of the particle for a truncated pyramidal particle with $b=2l_{ex}$ and a taper angle of $72°$, as a function of an aspect ratio R

The base diameter was fixed at $4l_{ex}$ or $4.5l_{ex}$, and the effect of aspect ratio was studied for different amounts of axial anisotropy (Figure 4.7) In contrast with flower-state particles, there is a gradual decrease in remanence with decreasing aspect ratio as the magnetization vectors become more tilted into the plane, but remanence is still significant even for particles with aspect ratios below 0.9. In the case of zero anisotropy, high aspect ratio particles ($R > 0.9$) show a remanence which saturates at 0.7 for $b = 4l_{ex}$, and at 0.6 for $b = 4.5l_{ex}$. Additionally, the remanence increases with increasing anisotropy.

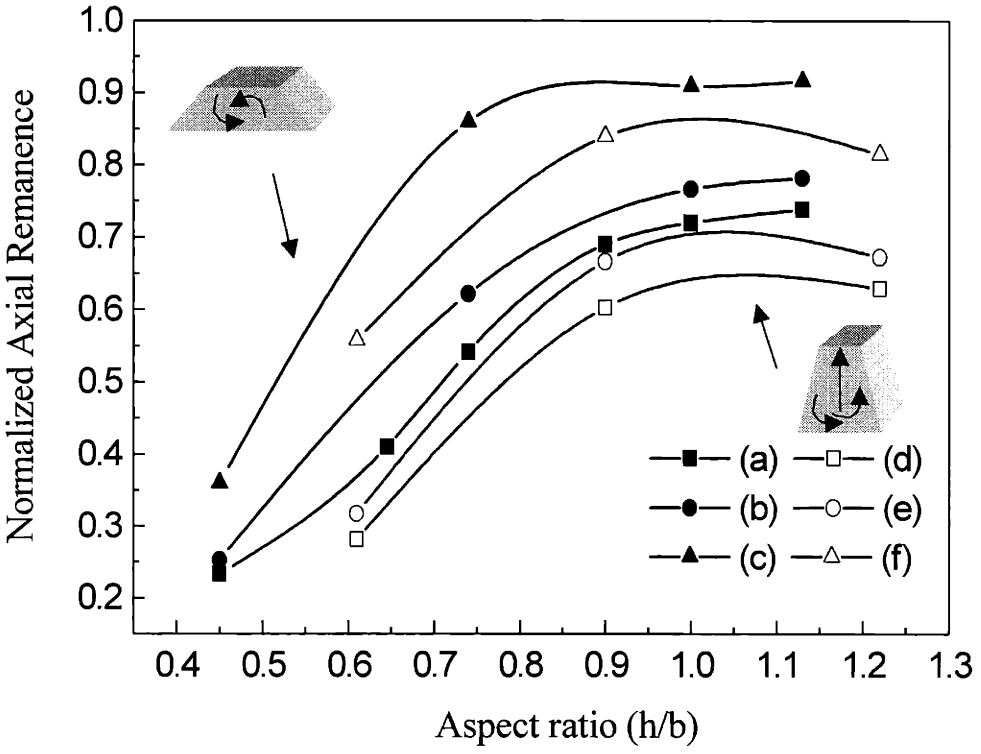

Figure 4.7: Calculated axial remanence for vortex particle, as a function of aspect ratio. (a) $b=4l_{ex}$, zero anisotropy; (b) $b=4l_{ex}$, anisotropy of $5\text{x}10^4$ erg/cm^3 along axis; (c) $b=4l_{ex}$, anisotropy of $2\text{x}10^5$ erg/cm^3 along axis; (d) $b=4.5l_{ex}$, zero anisotropy; (e) $b=4.5l_{ex}$, anisotropy of $5\text{x}10^4$ erg/cm^3 along axis; (f) $b=4.5l_{ex}$, anisotropy of $2\text{x}10^5$ erg/cm^3 along axis. Anisotropy values correspond to Ni particles.

4.2.4 Comparison with Experimental Results

Our simulation shows a transition from a flower state to a vortex state with increasing particle size. This behavior has been found in other geometries such as cubes, and prisms. However, the fact that even vortex states can have significant axial remanence at aspect ratios below 1 corresponds well to the experimental observations. The flower-to-vortex transition is predicted to occur at about 60 nm diameter for Ni, and 20 nm for Co with zero anisotropy. Even with zero anisotropy, Ni particles with ~80 nm diameter would show a helical magnetization state with significant perpendicular remanence. Moreover, due to the gradual decrease of remanence with increasing base diameter in vortex-state particles, Ni particles show dipolar magnetization pattern when $R > 0.65$. However, for Co, particles of 80nm diameter are predicted to have multi-domain or vortex states with very low remanence according to the model with zero anisotropy. The observation of dipolar magnetization states with high remanence in such particles is interpreted as a result of perpendicular anisotropy arising from the preferred (0001) crystal orientation, which is confirmed by X-ray diffraction.

Table 4.2 shows a comparison between experimental and calculated remanence data for selected samples. The dimensions of the model were adjusted to fit the measured particle dimensions as closely as possible. For nickel particles, the general trend in axial remanence is followed well, with an increase in remanence through the series as R increases and b decreases. However, the measured remanence values are higher than model values by typically 10 - 20%, possibly due to the presence of a small out-of-plane anisotropy in the nickel. The remanence was calculated for two different magnitudes of anisotropy described above, 5×10^4 erg/cm^3 and 2×10^5 erg/cm^3. The experimental data are better fit-

ted by higher anisotropy values, as the aspect ratio increases. For cobalt particles, the model particles are multi-domain with zero remanence without anisotropy, but anisotropy of $3x10^6$ erg/cm^3 stabilizes helical vortex states with remanence that increases rapidly with aspect ratio. Experimentally, the remanence does not increase with aspect ratio as fast as the model predicts. In real particles, the net anisotropy would be determined by the aspect ratio of the columnar grains and their degree of preferred orientation, and these probably vary with film thickness and with the geometry of the particles. The calculated remanence is a very sensitive function of the net anisotropy value used for the model, and the use of the same value for all modeled particles is a simplifying assumption. Moreover, the measured remanence value is an average value over millions of particles, which have slightly different microstructures among them. Ideally, it is closer to reality if we model particles with different microstructures with locally varying anisotropy values following the grain structures and then take averages over many of them. The purpose of modeling in this thesis is more about obtaining physical insight, so this method was not implemented due to its complexity.

4.3 Summary

In terms of application to patterned media, 80 nm particles in a 200nm period correspond to 19.5 Gbits/in^2 data density. Since this magnitude of data density has already been achieved even with conventional hard disk media, the period and particle size should be decreased further to constitute a useful patterned medium for high data density. For instance, a 50nm period, which maybe achieved by next generation AIL, would correspond to 250 Gbits/in^2. As the particle size becomes smaller than $3l_{ex}$, particles will show a nearly uniformly magnetized states (flower states), and the transition from out-of-plane to in-plane magnetization would occur at $R = 0.9$. For the evaporation/lift-off processes, it is hard to make high aspect ratio structures. Thus, it would be hard to make perpendicular

media in this case just relying on shape anisotropy. To make perpendicular media, more careful engineering of microstructure to achieve out-of-plane magnetocrystalline anisotropy would be required in this size regime. For example, Co/Pt multilayer can be a good candidate system for low aspect ratio perpendicular media.

	Experimental			Model					
Sample	Base *b* (nm)	Aspect ratio *R=h/b*	Rema-nence M_z/M_s	*b* (nm)	*h/b*	M_z/M_s for K_z =0	M_z/M_s for K_z =5x10^4 erg/ cm^3	M_z/M_s for K_z =2x10^5 erg/ cm^3	M_z/M_s for K_z =3x10^6 erg/ cm^3
N-1	122	0.45	0.12	121	0.45	0.08	0.08	0.18	
N-2	89	0.62	0.22	89	0.61	0.28	0.32	0.56	
N-3	84	0.65	0.40	84	0.65	0.36	0.42	0.72	
N-4	75	0.73	0.65	75	0.74	0.62	0.70	0.91	
N-5	89	0.90	0.79	89	0.90	0.60	0.67	0.83	
N-6	80	1.00	0.87	80	1.00	0.72	0.77	0.91	
N-7	91	1.21	0.81	90	1.22	0.63	0.67	0.81	
C-4	86	0.64	0.21	86	0.65	0.00			0.08
C-5	79	0.70	0.17	79	0.71	0.00			0.33
C-6	85	0.94	0.40	85	0.94	0.00			0.68

Table 4.2: Calculated and measured axial remanence M_z/M_s for evaporated particles. The calculations correspond to saturation magnetization M_s = 484 emu/cm^3 for Ni and 1422 emu/cm^3 for Co, and include different amounts of axial anisotropy K_u

Chapter 5

Electrodeposited Cylindrical Samples

In this chapter, the remanent states and switching field of electrodeposited cylindrical particles are studied by micromagnetic simulations and compared with experimental measurements. The effect of demagnetizing magnetostatic interactions and switching field spread on the squareness and the shape of hysteresis loops is studied with the help of an Ising-like interaction model. By comparing the maximum magnetostatic interaction field with the average switching field, the stability condition for patterned media is found, and used to determine the optimum spacing between nanomagnets.

5.1 Sample Discussion

Electrodeposited samples are cylindrical with a diameter equal to the diameter of holes in the template and height determined by deposition time. Large diameter cylinders often showed a concave top-surface, due to current crowding at the edges, but as the cylinder height approached the template thickness, the top surfaces tend to become convex. Most samples have a period of 200nm, except for Ni-1 and Ni-2, which have a period of 100nm. 100 nm period Ni samples are made by T. Savas in the NSL, and small diameter 200 nm period Ni samples are fabricated by Dr. M. Farhoud in the NSL by using negative resists. The saturation moments of both electrodeposited Ni and Co are lower than those of the pure elements, possibly due to impurity incorporation or surface oxidation. All the Ni samples showed a saturation moment (M_s) of 320 emu/cm^3, 0.66 times that of pure Ni. Co samples showed M_s of 1100 emu/cm^3, 0.77 times that of pure Co. CoP samples were made Dr. M. Shima with a current density of 0.15A/cm^2, and the sample reported in this study has an M_s of 500 emu/cm^3. We identify three different types of hysteresis loops, which

will be discussed in following subsection. Table 5.1 summarizes the dimensions and magnetic properties of the cylindrical particles used in this study.

Sample	Height h (nm)	Diameter d (nm)	Period (nm)	Aspect ratio R=h/d	Loop type	H_c IP (Oe)	H_c OP (Oe)	Squareness in plane	Squareness out of plane	H_i
Ni-01	115	57	100	2.02	A	106	710	0.07	0.88	94
Ni-02	164	75	100	2.19	A	72	540	0.06	0.49	232
Ni-03	125	92	200	1.36	A	27	240	0.04	0.66	33
Ni-04	220	92	200	2.40	A	46	392	0.03	0.70	58
Ni-05	251	108	200	2.32	A	185	339	0.16	0.55	92
Ni-06	209	108	200	1.94	A	63	276	0.01	0.63	77
Ni-07	198	108	200	1.83	A	51	223	0.03	0.55	73
Ni-08	66	161	200	0.41	B	215	200	0.32	0.18	54
Ni-09	70	95	200	0.73	B	110	44	0.48	0.05	20
Ni-10	109	142	200	0.77	C	145	139	0.11	0.10	69
Ni-11	214	144	200	1.49	C	43	53	0.11	0.02	139
Ni-12	236	160	200	1.48	C	71	77	0.11	0.04	190
Ni-13	190	155	200	1.22	C	70	102	0.08	0.07	143
Co-1	130	184	200	0.70	C	44	161	0.02	0.02	475
Co-2	226	176	200	1.28	C	61	132	0.017	0.022	756
CoP-1	160	100	200	1.6	C	20	110	0.015	0.052	79

Table 5.1: Physical and magnetic characteristics of the electrodeposited samples, H_i computed assuming uniform magnetization perpendicular to the plane.

5.2 Experimental Observation

We observe three different types of hysteresis loops, which we label as Type A, B, and C loops.

1) Type A loops: loops with large squareness, high coercivity, and a sheared shape in the out-of-plane direction, while the in-plane direction shows low coercivity and remanence characteristic of a hard axis. This type A loop is consistent with the behavior of an array of interacting dipoles oriented perpendicular to the plane, which can be verified by MFM. MFM results show that each pillar is magnetized parallel to its length, and shows either dark or light contrast depending on whether it is magnetized 'up' or 'down.' Representative MFM images are shown in Figure 5.1. Among our samples, only nickel samples with a small diameter and an aspect ratio larger than 1 show this behavior. Figure 5.2 and Figure 5.3 show scanning electron micrographs of the type A samples and their room temperature hysteresis loops measured parallel and perpendicular to the substrate. For this category of samples, coercivity increases with a decreasing diameter and increasing aspect ratio.

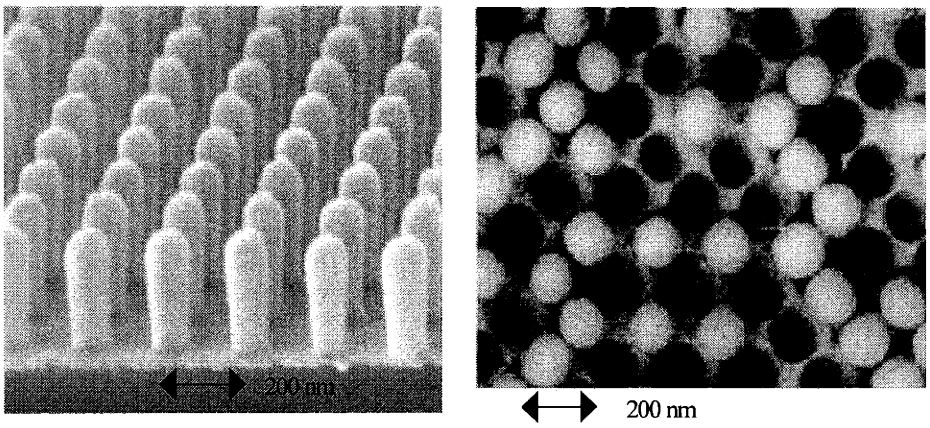

Figure 5.1: An array of electrodeposited Ni pillars, with diameter 92nm and height 220nm. The magnetic force microscopy image shows that each pillar is magnetized 'up' (light) or 'down' (dark). Figure is due to Dr. M. Farhoud

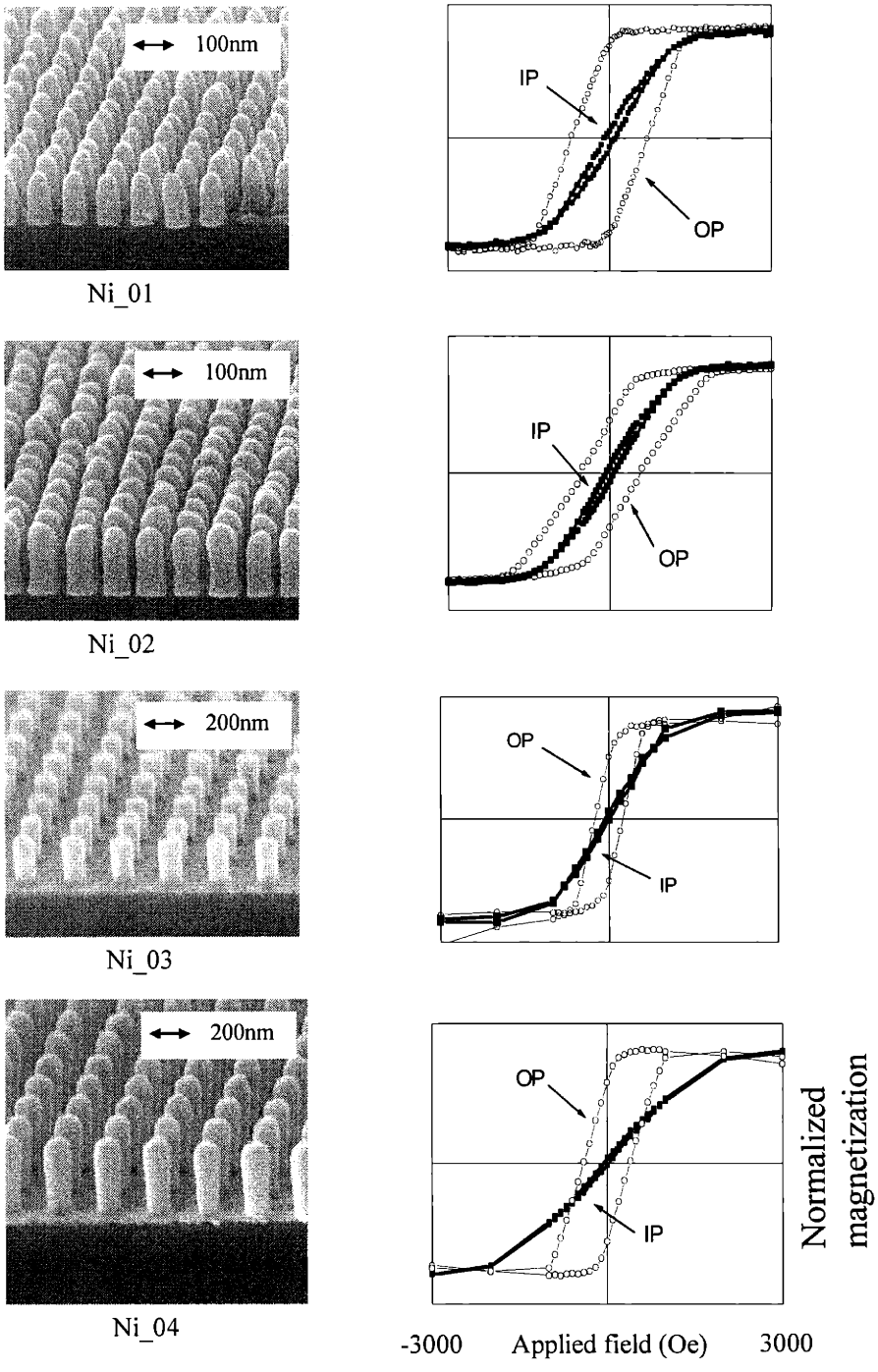

Figure 5.2: Scanning electron micrographs and corresponding hysteresis loops of type-A electrodeposited Ni samples (1)

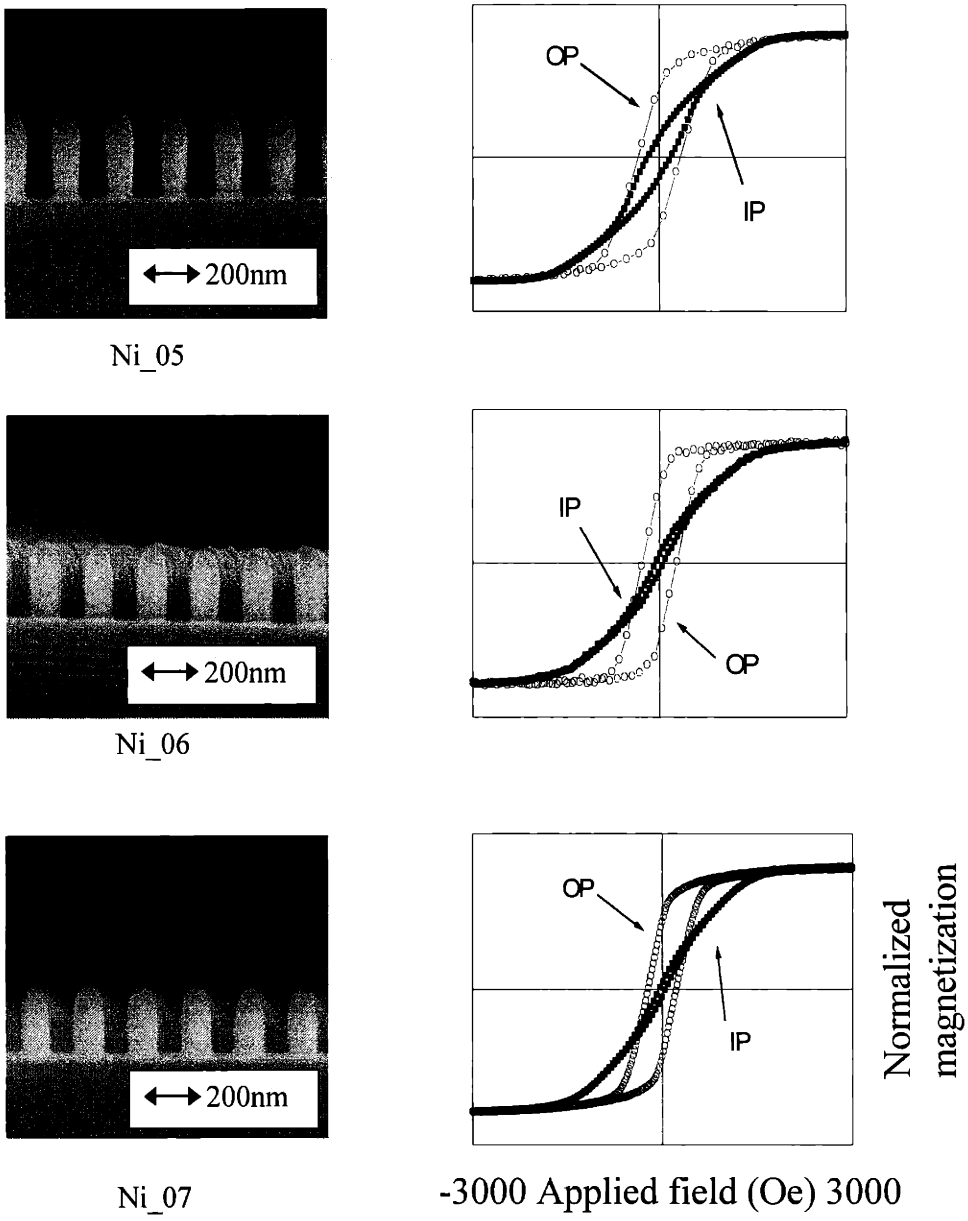

Figure 5.3: Scanning electron micrographs and corresponding hysteresis loops of type-A electrodeposited Ni samples (2)

2) Type B loops: Low aspect ratio pillars ($R < 1$) with small diameters show hysteresis loops characteristic of an easy axis in plane, with a hard axis parallel to the length of the pillars. The circular symmetry of particles would suggest free rotation of magnetization in the plane with zero in-plane coercivity, but the samples do show significant in-plane coercivity, presumably due to pinning of the magnetization by inhomogeneities, surface roughness, etc. Among the samples, only nickel samples with a small diameter and an aspect ratio less than 1 show this behavior. Figure.5.4 shows scanning electron micrographs of the type B samples and their room temperature hysteresis loops measured parallel and perpendicular to the substrate.

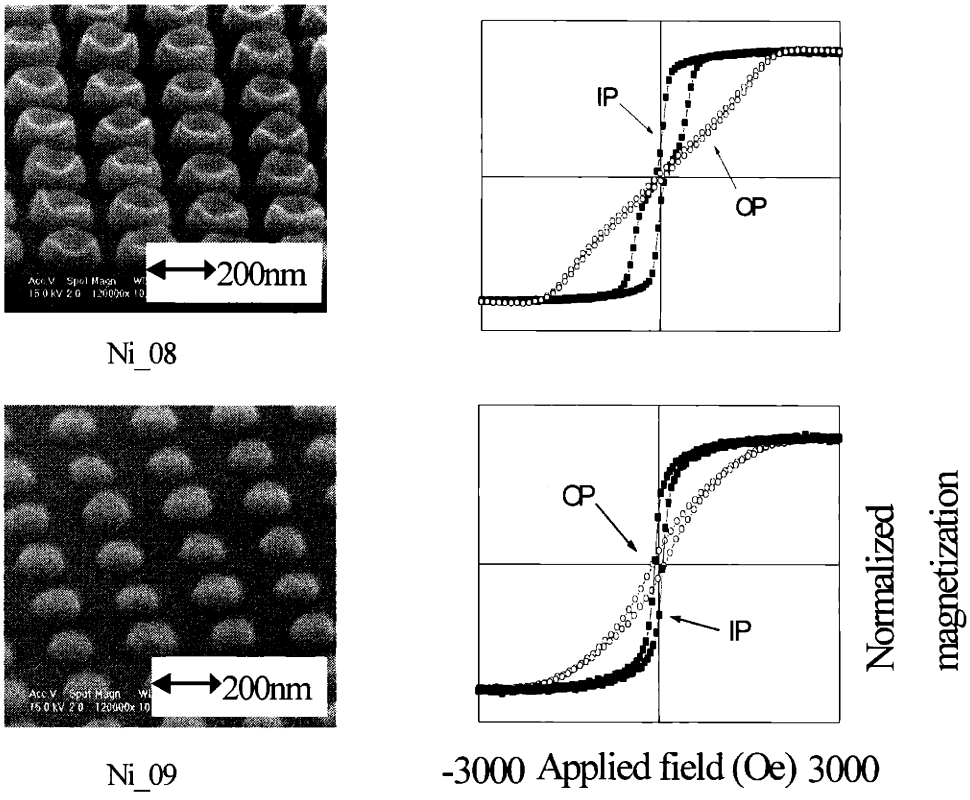

Figure 5.4: Scanning electron micrographs and corresponding hysteresis loops of type-B electrodeposited Ni samples

2) Type C loops: The majority of the samples show *M-H* loops in which both in-plane and out-of-plane magnetization directions have low coercivity and remanence. The field required to saturate the magnetization in either direction is of order 1000 Oe, and depends on the aspect ratio and spacing of the pillars. These samples also show little contrast in MFM images. Among the samples, large diameter Ni samples and all the Co and CoP samples belong to this category. Figure 5.5 shows scanning electron micrographs of the type C Ni samples and their room temperature hysteresis loops measured parallel and perpendicular to the substrate. Figure 5.6 shows the same sets of data for the Co and CoP samples.

To interpret these results, micromagnetic simulations are carried out in the following section.

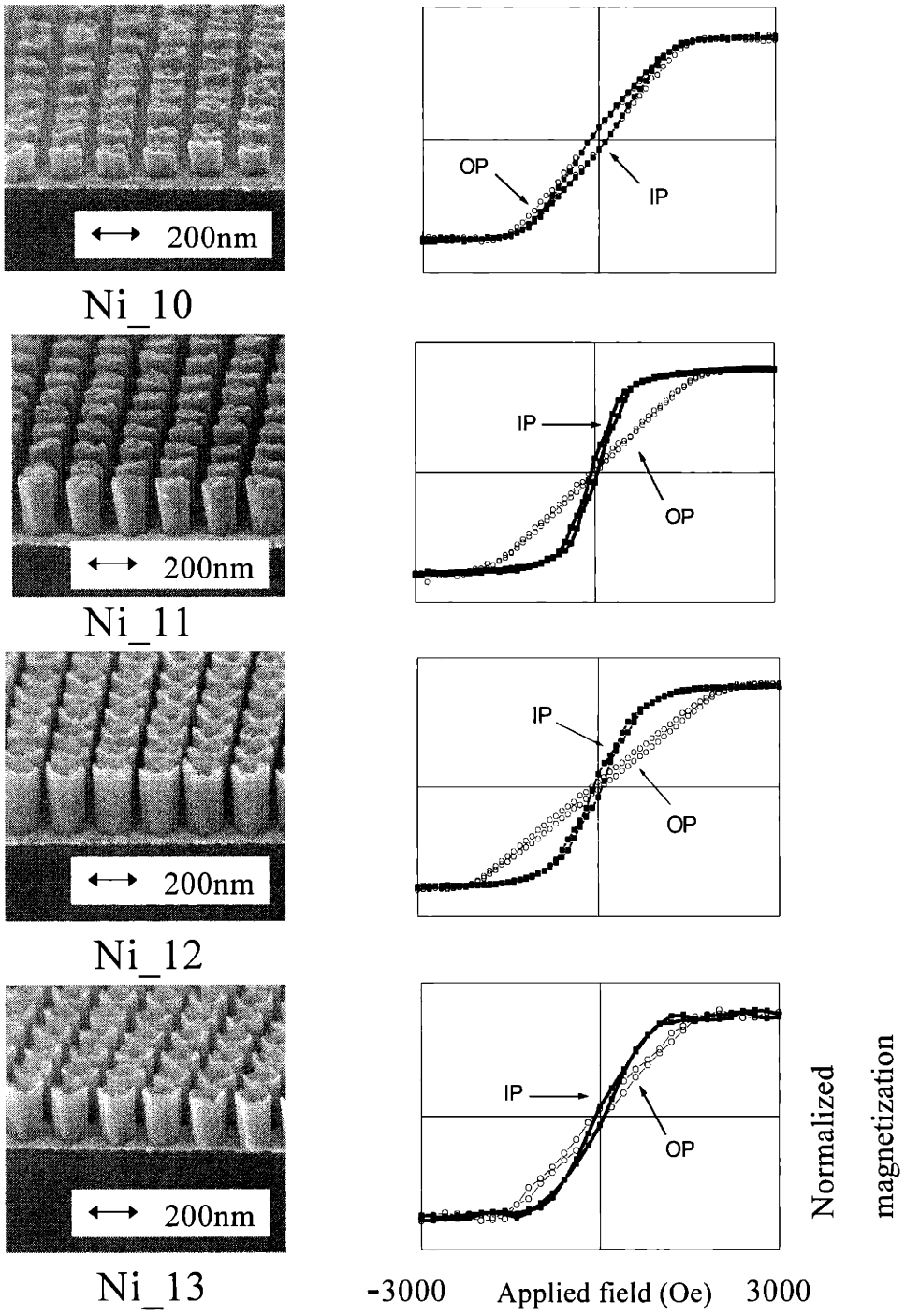

Figure 5.5: Scanning electron micrographs and corresponding hysteresis loops of type-C electrodeposited Ni samples

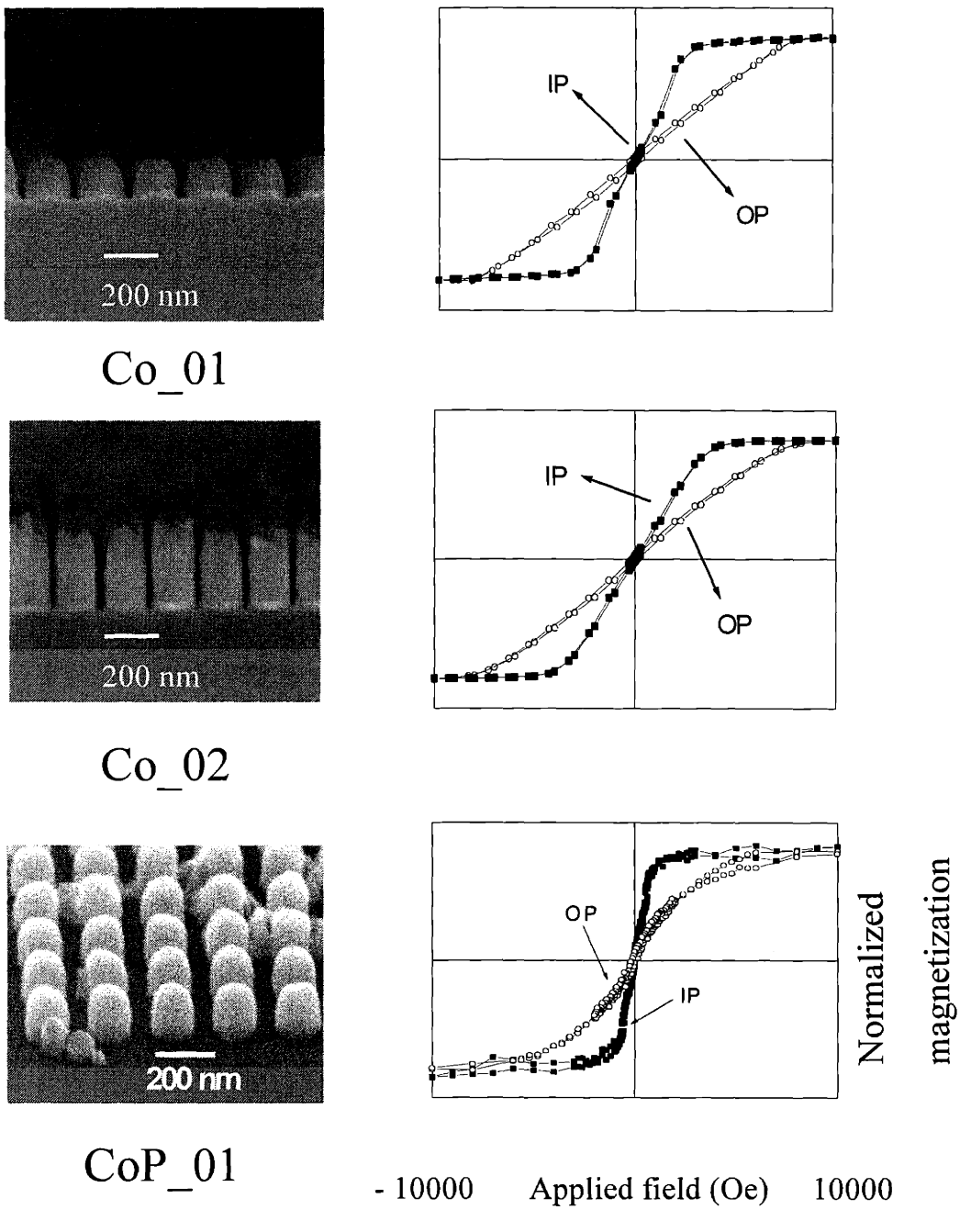

Figure 5.6: Scanning electron micrographs and corresponding hysteresis loops of type-C electrodeposited Co and CoP samples

5.3 Individual Cylinder - Remanent State Studies

5.3.1 Modeling Details

A particle is modeled as a homogeneous cylinder. First, we neglect in-particle magnetocrystalline anisotropy. This assumption is reasonable for polycrystalline particles, provided randomly-oriented crystalline anisotropy averages out. Moreover, the preferred orientation is weak for electrodeposited Ni samples, the cubic anisotropy of Ni at room temperature is small compared to the shape anisotropy, and the grains of Ni samples are fine and equiaxed, so zero-anisotropy is a good first-order assumption for Ni particles. CoP particles are amorphous, so it is natural to assume that these particles do not have any magnetocrystalline anisotropy. For Co particles, the effect of anisotropy is studied later on by adding homogeneous uniaxial anisotropy along the long axis of the particle.

The particle is represented by $N_x \times N_y$ cubic elements in the *xy* plane for the base of the particle. Along *z*, perpendicular to the base, N_z elements represent the height. The volume of the particle was divided into between 900 and 20000 elements, with N_x=N_y=21 or 31, and N_z = 1- 63 depending on the desired aspect ratio. Length scales are again normalized with respect to the exchange length. An exchange constant of $A = 10^{-6}$ erg/cm was used for Ni, CoP, and Co particles. Since measured saturation magnetizations M_s of both Ni and Co were lower than those of the pure elements, the experimentally measured values of 320 and 1100 emu/cm^3 were taken for Ni and Co. For CoP particles, M_s changes with P content, so the measured value was used for the model. To study the effect of uniaxial anisotropy, values of uniaxial magnetocrystalline anisotropy K_u in the range from zero to 4.5x10^6 erg/cm^3 (corresponding to pure Co) parallel to the particle axis were used in different calculations. The anisotropy is normalized with respect to the stray field coef-

ficient (= $2\pi M_s^2$), and given as a quality factor Q (= $K_u/(2\pi M_s^2)$), which represents the relative strength of anisotropy over the demagnetization effect. Q = 0.3542 corresponds to the case of single-crystal cobalt [36].

5.3.2 Effect of Particle Size on Remanence

1) Aspect ratio, $R > 0.9$

Three different aspect ratio, 1.5, 2.1, and 3.0 are simulated with zero anisotropy. It was found that cylindrical particles behave qualitatively similar to pyramidal particles analyzed before. In Figure 5.7, the axial remanence is shown as a function of normalized diameter.

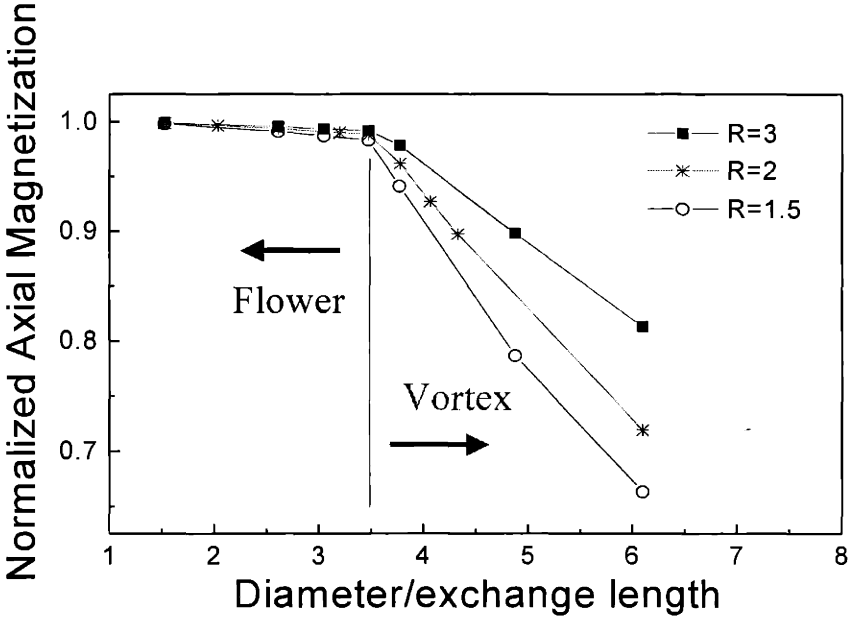

Figure 5.7: Calculated axial remanence for cylindrical particles after axial saturation, as a function of normalized base diameter. Three different aspect ratios, 1.5, 2.1, and 3.0 are simulated.

A cylinder with a diameter smaller than $3.5l_{ex}$ shows an "out-of-plane flower" state where remanence is very close to 1 and magnetization is mostly parallel to the long axis

except for small deviations at the corners. As the diameter becomes bigger than $3.5l_{ex}$, vortices develop from the ends of the cylinder. The spins at the center are still aligned with the long axis of the particle, but the spins at the ends become tilted into the sample plane.

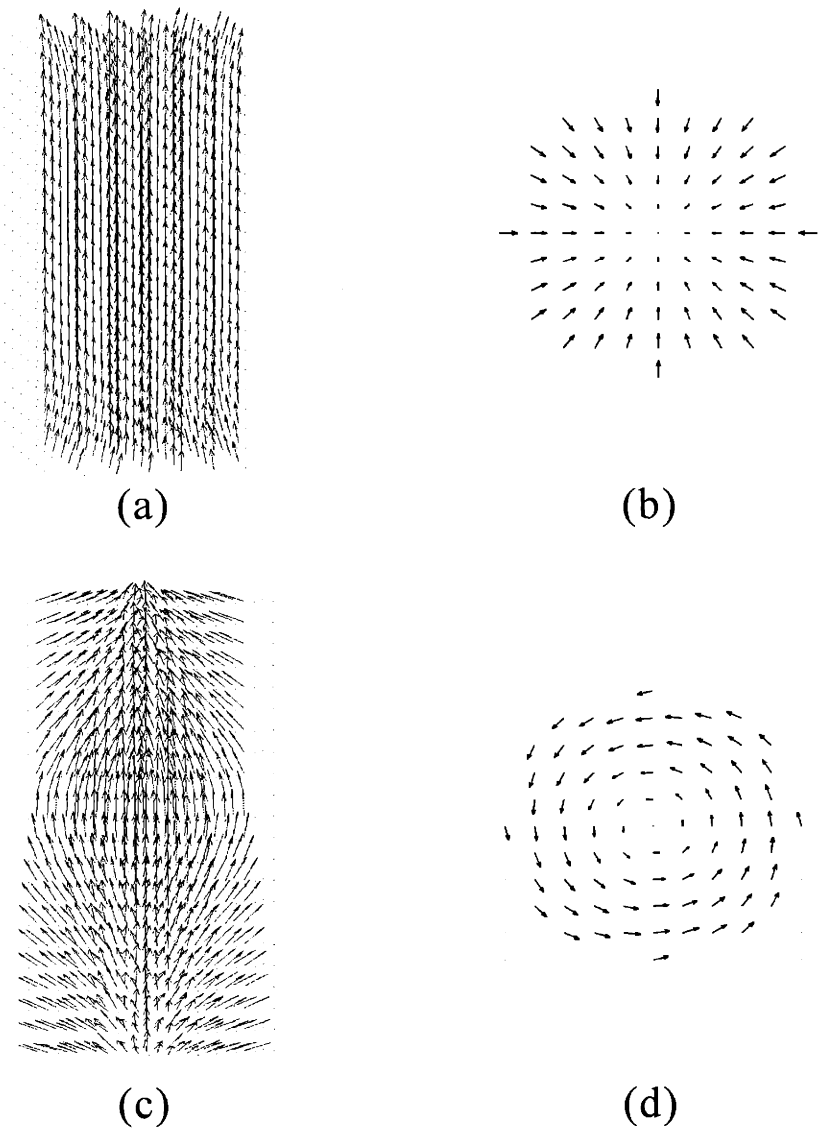

Figure 5.8: 3D vector plots of remanent states and cross-sections (a) "Out-of-plane flower" state, $R = 2.1$, d/l_{ex}=2.61; (b) Same particle as (a) showing the magnetization in the base plane; (c) "Vortex" state, $R = 2.1$, d/l_{ex}=6.1; (d) Same particle as (c) showing the magnetization in the base plane

Figure 5.8 shows 3D vector plots and cross-sections of calculated remanent states. As the particle diameter increases, the magnetization near the particle-ends tilts more into the sample plane and vortices formed at both ends expand into the particle, causing a gradual decrease in the axial remanence. The decrease in remanence is more gradual as R increases, as shown in Figure 5.7.

2) Aspect ratio < 0.9

It is well-known that a uniformly magnetized cylinder goes through a reorientaional transition from out-of-plane to in-plane magnetization when R becomes 0.9065 [35]. For cylinders with small diameter ($d<3.5l_{ex}$), we observed the same transition from the "out-of-plane flower" state to the "in-plane flower" state around R= 0.9. Two different aspect ratios of 0.7 and 0.03 are selected to investigate the effect of aspect ratio on the critical diameter for the "in-plane flower" to "vortex" transition.

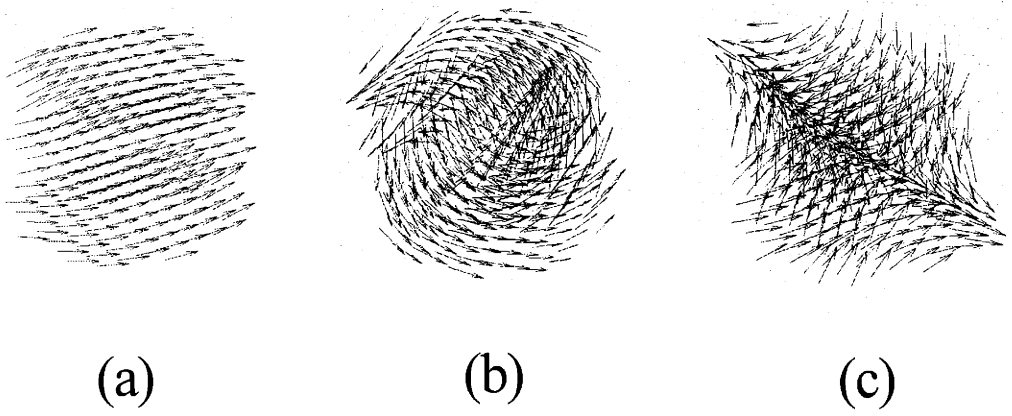

Figure 5.9: 3D vector plots of remanent states for R = 0.7 (a) "In-plane flower" state, d/l_{ex}=2.9; (b) "Vortex" state, d/l_{ex}=5.8; (c) "Multi-domain" state, d/l_{ex}=10.2.

Figure 5.9 shows three different types of remanent states calculated for $R = 0.7$. Interestingly, now vortices lie perpendicular to the base plane, contrary to those formed parallel to the base plane in taller cylinders ($R > 0.9$). It might be due to the difference in initial configurations. We started from magnetizations saturated along the base plane for low aspect ratio structures and but for taller cylinders, the starting configuration was to have the magnetization saturated perpendicular to the base plane. The other difference with regard to taller cylinder is that the critical diameter for the "in-plane flower" to "vortex" transition increases to $3.9l_{ex}$. Cylinders larger than $10l_{ex}$ show multi-domain remanent states as shown in Figure 5.9.

To investigate the extreme case of a very short cylinder, $R = 0.03$ is chosen. Again, we identified "in-plane flower" and "vortex" states. Due to the confinement along the cylinder axis, now the vortex lies parallel to the base plane. The calculated remanent states are shown in Figure. 5.10. The critical diameter for the transition now further increases to $11.9l_{ex}$. It seems that this critical diameter for the transition is a smooth function of aspect ratio. The reason for not seeing this kind of dependence on aspect ratio for taller cylinders might be that we simulated relatively small ranges of aspect ratios for $R > 1$. Due to the fabrication scheme, it is hard to make the aspect ratio of the particles larger than 3, so we did not consider higher aspect ratio structures.

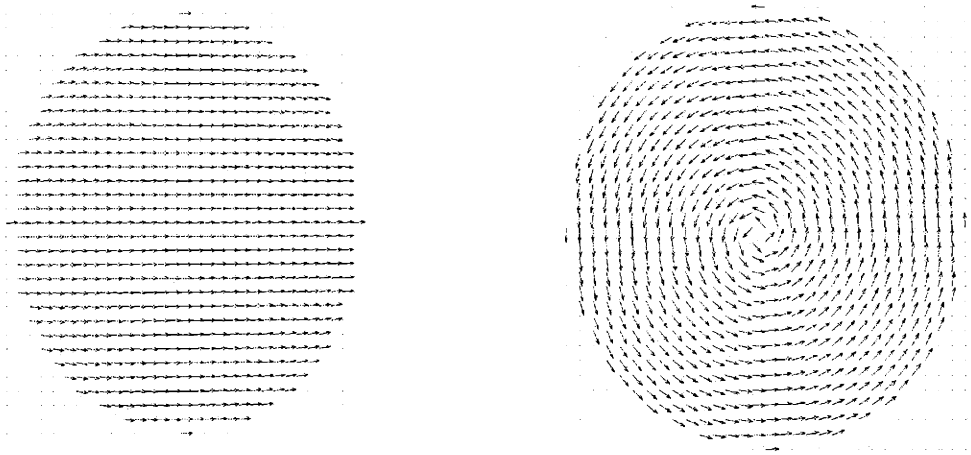

Figure 5.10: 3D vector plots of remanent states for R = 0.03 (a) "In-plane flower" state, d/l_{ex}=7.0; (b) "Vortex" state, d/l_{ex}=15.0

5.3.3 Effect of Uniaxial Anisotropy on Remanence

Adding uniaxial anisotropy with an easy axis parallel to the axis of the cylinders stabilizes the "flower" state and makes the "flower" to "vortex" transition occur at larger diameters. To obtain quantitative results, three different aspect ratios, 1.5, 2.1, and 3.0 are simulated with different values of uniaxial anisotropy. The results are shown in Figure 5.11. As Q increases to 0.3542, the critical diameter for the transition increases from $3.5l_{ex}$ to $16.8l_{ex}$ for R = 1.5 and $19.9l_{ex}$ for R= 3.0.

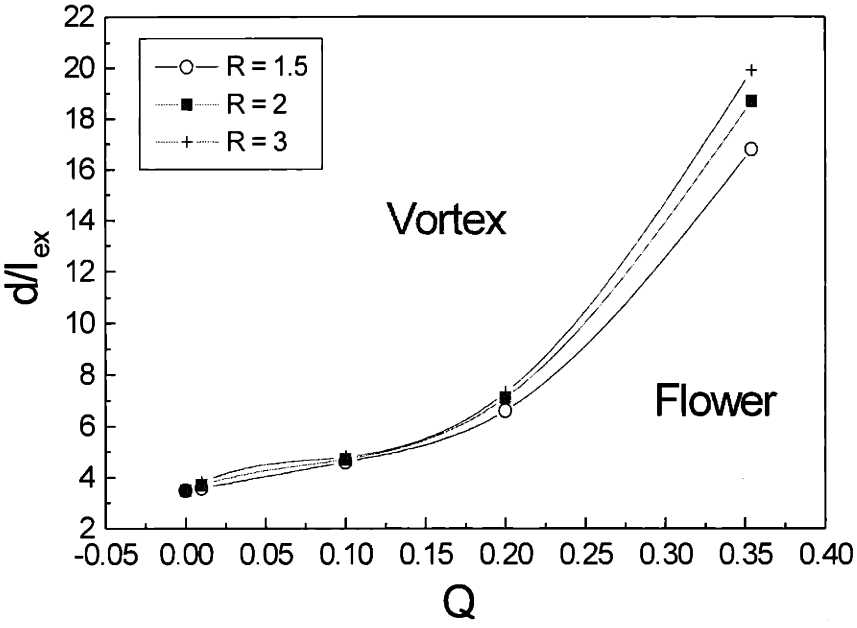

Figure 5.11: Calculated normalized critical diameters for the "flower" to "vortex" transition for cylindrical particles as a function of quality factor. Three different aspect ratios, 1.5, 2.1, and 3.0 are simulated.

5.3.4 Comparison with Experimental Results

For the zero anisotropy case, a magnetic phase diagram was built by defining the boundary between "flower" and "vortex" states as a function of aspect ratio and normalized diameter. The resulting plot is shown in Figure 5.12. To compare the experimental results for Ni and CoP with these model results, data from the measured arrays is superposed on Figure 5.12. The normalized diameter for each particle is calculated using an exchange length derived from the measured saturation moment, with an exchange constant of $1x10^{-6}$ erg/cm. Each data point is coded according to the hysteresis loop type. There is a good correlation between Type A loops and the out-of-plane flower state region,

Type B loops and the in-plane flower state region, and Type C loops with the vortex region.

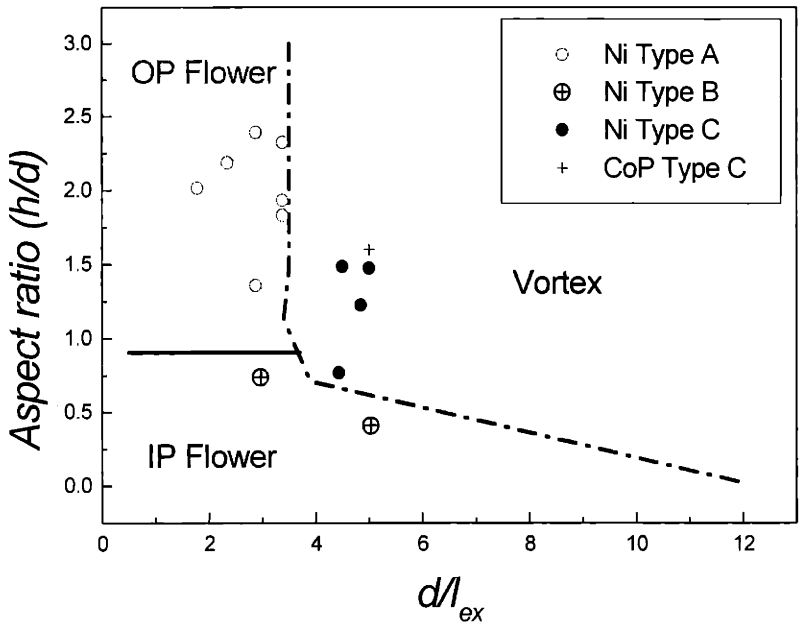

Figure 5.12: A magnetic state phase diagram for nanomagnets plotted as a function of the aspect ratio h/d and normalized diameter d/l_{ex} of nanomagnet. Experimental datapoint is coded according to the hysteresis loop type.

Deviations from this model can occur for two reasons. First, the presence of inhomogeneities such as grain boundaries, and magnetocrystalline anisotropy, can affect the behavior of the particles. We found earlier that for evaporated Co particles, magnetocrystalline anisotropy significantly increased the out-of-plane remanence, and increased the critical size for the "flower" to "vortex" transition. Columnar grain shapes in these particles also caused some additional out-of-plane anisotropy. However, in electrodeposited cylinders, magnetocrystalline anisotropy and grain shape effects would be less important

than for the evaporated samples because the preferred orientation is weak, and the grains are fine and equiaxed instead of being columnar.

Another effect is that interactions among particles can cause magnetic reorientation of the particle easy axis direction from out-of-plane to in-plane even for $R > 0.9$ when particles are closely packed. This will be explained in detail in the following section.

However, despite these caveats, we have good agreement between loop shape and the calculated magnetization phase diagram. This supports the interpretation that A-type loops originate from flower-state particles.

5.4 Individual Cylinder - Switching Field Studies

Since Type B and C particles are not useful for perpendicular data storage media, we are mainly interested in the switching characteristics of Type A particles, which are uniformly magnetized along the long axis of the cylinder. The coercivity taken from the hysteresis loop measurements can be thought of as an average switching field of the particle array. Experimentally, the average switching field increases with decreasing particle diameter and increasing aspect ratio. The effect of geometry on the average switching field is studied by micromagnetic simulations, using a general FMM code developed by Dr. C. Seberino and Prof. Neal H. Bertram at UCSD. We started from the magnetization of all the cells aligned in the direction of the field, which is large enough to saturate the particle. The applied field is reduced by preset steps toward the reversal direction until the integral magnetization value computed over the particle volume changes its sign. The field at which the magnetization changes its sign is defined as a calculated switching field. Since we are only dealing with Ni particles in this section, the magnetic properties for Ni are summarized in Table 5.2.

	4.2 K	300 K(room temperature)
Crystal Structure	FCC	
M_s	510 emu/cm^3	485 emu/cm^3
K_1	-12 x 10^5 erg/cm^3	-4.5 x 10^4 erg/cm^3
K_2	3.0 x 10^5 erg/cm^3	-2.3 x 10^4 erg/cm^3
Curie temperature	627 K	

Table 5.2: Magnetic properties of Ni, Taken from [37]

5.4.1 Effect of Particle Size

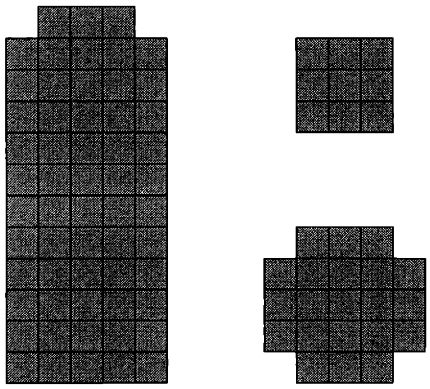

Figure 5.13: Cross-section of discretization used to model bullet-shaped particles

Among the samples shown in Table 5.1, TEM shows that Ni-01 and Ni-02 are single grain. Moreover, they have similar aspect ratios, so these particles were chosen to be modeled in detail. According to X-ray results on blanket-film samples, the <111> axis lies parallel to the long axis of these particles. We are interested in simulating the room

temperature switching field dependence on the size of particles. However, micromagnetics is essentially a zero temperature model, and thermal effects are ignored in the calculation. In practice, zero temperature micromagnetics is a good approximation to many systems at room temperature as well, because thermal energy is usually much smaller than the magnetic energies of the system. However, as particle size becomes small, thermal energy can be comparable to the effective barrier height for switching. Ideally, if magnetic parameters do not change with the temperature and thermal energy can be ignored, there would be no temperature dependence of switching field. Thus, we did low-temperature hysteresis measurements on Ni-01 and Ni-02 to validate our comparison of the zero-temperature model with the room temperature results. Quite contrary to our expectation, measured coercivity almost doubles as temperature decreases from room temperature as shown in Figure 5.14. This change in coercivity can be due to 1) thermally assisted switching, or 2) a change in magnetic properties as shown in Table 5.2. The saturation moment does not change that much with temperature. However, the cubic anisotropy constant at 4.2K shows a 30 times increase from its room temperature value, and a change in sign. Due to this change in sign, the easy axis of Ni changes from <111> at room temperature to <110> at 4.2K. This can be the reason why we see a strong temperature dependence of switching field, but it is hard to verify how much it contributes to the lowering of the switching field. Micromagnetic simulations were performed to understand this phenomenon more quantitatively.

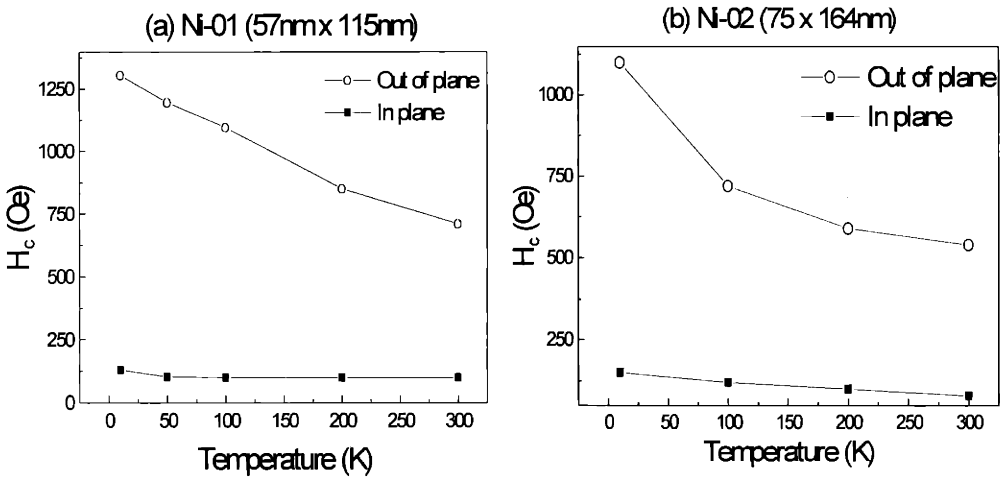

Figure 5.14: Temperature dependence of coercivity for selected samples (Ni-01 and Ni-02)

Particles are modeled as 5x5x12 bullet-shaped cylinders with aspect ratio of 2.4. The schematic of the discretization is shown in Figure 5.13. Two cases, 1) one with zero anisotropy and 2) the other with the cubic anisotropies of Ni at 4.2K, were simulated. As shown in Figure 5.15, the switching field monotonically decreases with increasing normalized diameter. The inclusion of cubic anisotropy makes the switching field increase two-fold for particles around $3l_{ex}$. To make a comparison with experimental data, the following is assumed.

1) From TEM results, we know there exists a 5nm oxide shell around the Ni particles. To calculate the effective magnetic volume, this shell volume is subtracted from the particle size measured by SEM.

2) Assuming that the lowering of M_s is just due to the surface oxidation, literature values for pure Ni, shown in Table 5.2, are used for both saturation moment and cubic anisotropy constants.

3) The exchange constant for Ni is assumed to be 0.8 x 10^{-6} erg/cm.

Experimental data are superimposed on Figure 5.15. The agreement seems reasonably good. Zero anisotropy simulation results correlate quite well with the room temperature measurements, and cubic anisotropy simulation results correspond well to the low temperature measurements. Thus, the origin of switching field enhancement with decreasing temperature is most likely due to the change of magnetic properties of Ni with temperature.

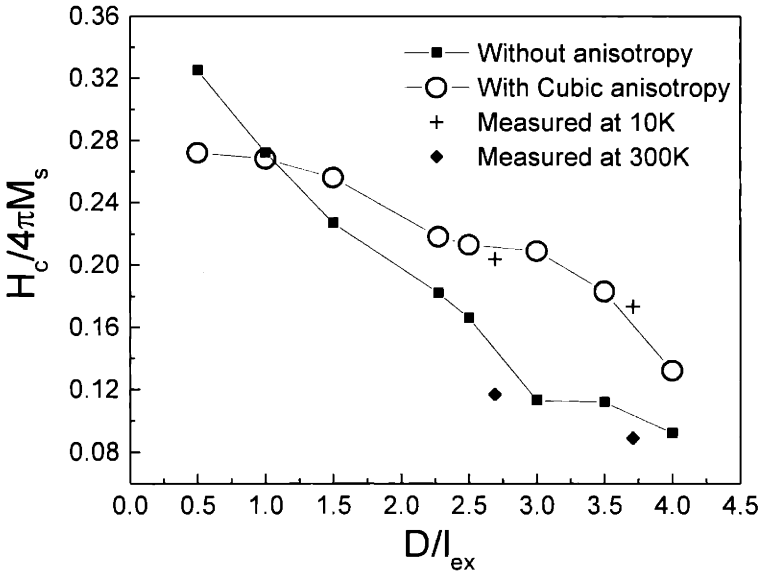

Figure 5.15: The dependence of switching field on the size of particles. R is fixed to 2.4.

5.4.2 Effect of Aspect Ratio

Because Ni-05, Ni-06, and Ni-07 have the same diameter and different aspect ratios, these particles are chosen to study the effect of the aspect ratio on the switching field. Particles are modeled as 7x7x12, 7x7x14, and 7x7x16 cylinders. Due to the polycrystalline nature of samples, zero anisotropy is assumed. The following two cases are simulated for comparison with the experiment. The exchange constant is assumed to be 1.0×10^{-6} erg/cm for all the cases.

Case 1) M_s of pure Ni (485 emu/cm^3) and the effective diameter (actual particle diameter - thickness of oxide shells (5nm on the one side + 5nm on the other = 10nm in total) are used.

Case 2) Measured M_s values (320 emu/cm^3) and the actual physical particle diameter are used.

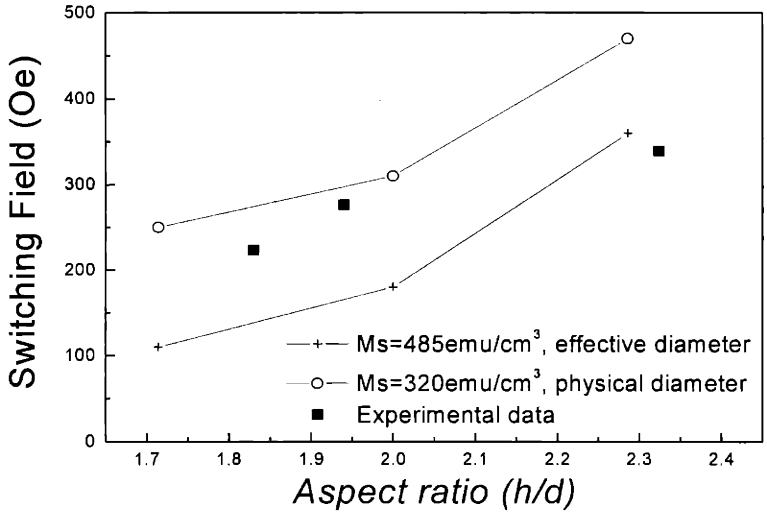

Figure 5.16: The dependence of switching field on the aspect ratio of particles

The simulated results are compared with the experimental data in Figure 5.16. The dependence of switching field on the aspect ratio can be verified for the particles in this size regime, and the simulated results qualitatively agree well with the experimental results.

However, the measured data lies between the cases considered in this simulation and the simulated results show steeper slopes compared to experimental results. This might be due to the simplified assumptions of homogeneous cylinders. The deviations between simulations and measurements can be due to the following effects

1) The presence of inhomogeneities such as grain boundaries, and magnetocrystalline anisotropy variation over the particles. To be exact, the microstructure of particles also has to be considered.

2) The uncertainty in the value of the exchange constant and saturation moment for the particle. Although the order of magnitude and the value for pure elements are reported in the literature, real particles can have different values for these fundamental magnetic parameters.

3) The effect of averaging over particle arrays. We are comparing the average values over particle arrays with the simulation results on an isolated particle. The microstructure and geometry vary among particles, and they affect the switching characteristics of particles significantly.

5.4.3 Nonuniformity of Switching Field

M. Abraham of Prof. R. J. Ram's group conducted MFM studies of the microscopic switching characteristics of Ni-01 [38]. The intrinsic distribution of switching field was obtained from the measurements, and the switching field was shown to follow a Gaussian distribution with a mean value of 710 Oe (corresponding to the coercivity of the array) and

a standard deviation, ΔH_{sw} of 105 Oe. The apparent standard deviation increases to 276 Oe, if interactions among particles are not taken into account. Several other studies on particle arrays have shown substantial ranges of switching fields [39, 40], although the contributions from interactions have not been separated from intrinsic variability among particles. Part of this intrinsic variability can be due to variations of the height and diameter of particles. However, particles even with same geometry were found to have different switching field in this study, thus the origin of this variability is presumed to be microstructure differences among particles in the array. The effect of this switching field distribution and interactions on the shapes of hysteresis loops are discussed in the following section.

5.5 Effect of Interaction on the Collective Behavior of Particle Arrays

5.5.1 Magnetostatic Interactions

To quantify magnetostatic interactions in the arrays, we approximate nanomagnets by dipoles or uniform prisms, and calculate the interaction field at the center of each particle. Using a dipole approximation, the nearest neighbor interaction field between parallel dipoles can be computed as

$$H_i = \frac{M_s V}{p^3} \tag{5.1}$$

where M_s is the saturation moment of the particle, V the particle volume, and p the period of the particle arrays. The computed values are shown in Table 5.1. In a square array, the maximum interaction field experienced by one particle from all its neighbors if they are magnetized in the same direction is $9 \cdot H_i$ [6]. For Ni-01, this is 846 Oe, which is slightly larger than the average switching field of 710 Oe. This means that magnetization patterns in Ni-01 will be relatively stable with respect to interactions from their neighbors.

Only the small fraction of particles which have the lowest switching fields can switch at zero field under the influence of their neighbors ($9 \cdot H_i$), resulting out-of-plane squareness of 0.88. In contrast, Ni-02 has a maximum interaction field of 2088 Oe, which is much larger than the average switching field of 540 Oe, thus particles can spontaneously reverse their magnetizations due to the interaction field from their neighbors. The out-of-plane squareness is therefore 0.49 for Ni-02, because 25% of the particles reverse spontaneously after a saturating field is removed. If we push this argument a little further, the squareness of the hysteresis loop can decrease to nearly zero if interactions are much larger than the average switching field.

For square dipole arrays, the lowest energy configuration is known to be a 'checkerboard' pattern where the total magnetostatic energy is minimized by having adjacent particles with antiparallel magnetization. This may partly explain why Type C samples have a low squareness. Due to their large size compared to the exchange length, their average switching field is low and their interaction field is high, thus resulting in a tendency to align their magnetizations antiparallel. Moreover, interactions among the cylinders can cause a reorientation of the array's easy direction from out-of-plane to in-plane [41]. Due to the magnetostatic coupling between cylinders, the critical aspect ratio for in-plane to out-of-plane magnetic reorientation is increased from 0.9065 for isolated cylinders to 2.81 for closed packed cylinders (where the spacing between cylinders is equal to zero.) [41,42]. For our samples, the spacings between cylinders are large enough to prevent this magnetic reorientation from happening, but this calculation clearly shows the importance of controlling magnetostatic coupling between cylinders. To investigate the combined effect of switching field nonuniformity between cylinders and magnetostatic interaction on the shape of the hysteresis loops, a simple interaction simulation is performed in the following section.

5.5.2 Modeling Hysteresis for Type A Particles

The arrays were modeled as 12×12 two-dimensional arrays of particles with square hysteresis loops, with a Gaussian distribution of switching fields [43]. A 12×12 array was chosen for most calculations because larger arrays gave similar results, while smaller arrays showed discrete jumps due to the finite number of elements. The magnetization of the arrays is set perpendicular to the plane of the array. The particles interact magnetostatically, with interaction fields calculated using a dipole approximation or a rectangular prism approximation. The dipole approximation gives the upper bound for the interaction field. However, for closely spaced particles, it has been shown that the dipole approximation overestimates the interaction field by as much as 17.4%, especially for neighbors at shorter distance [44], so we approximate Ni cylinders as rectangular prisms with uniform magnetization and calculate the interaction field H_i, using an analytical formula obtained by Joseph et al [45].

$$\begin{aligned} H_i = -2M_s[&\operatorname{acot}(f(x,y)) + \operatorname{acot}(f(-x,y)) \\ &+ \operatorname{acot}(f(x,-y)) + \operatorname{acot}(f(-x,-y))] \end{aligned} \tag{5.2}$$

where

$$f(x,y) = \frac{[(a-x)^2 + (a-y)^2 + c^2]^{\frac{1}{2}} c}{(a-x)(a-y)} \tag{5.3}$$

M_s is the saturation moment, x and y the coordinates along the axes of the array from the center of the particle being considered, a the radius, and c the half height of the particles.

A simple iteration method is used to reconstruct a major hysteresis loop. The particles only interact magnetostatically, so the effective field acting on each particle is just a sum of the applied field and the interaction field from all its neighbors. If the effective field is larger than the switching field for a particular particle, the magnetization of the particle is reversed, and the interaction fields for all particles are updated. This is continued until none of the particles changes. Once the equilibrium state is obtained, the total magnetization of the array is calculated by summing up the magnetization of individual particles. Then the applied field is changed by a preset step and these procedures are repeated until the entire hysteresis loop is calculated. To compare calculated loops with experimentally measured data, the particle volume, spacing, easy axis direction, saturation moment, and average switching field are assigned from the values determined experimentally by VSM and SEM. The only adjustable parameter is the standard deviation, ΔH_{sw} of the particle switching fields, but this can also be confirmed by MFM measurements.

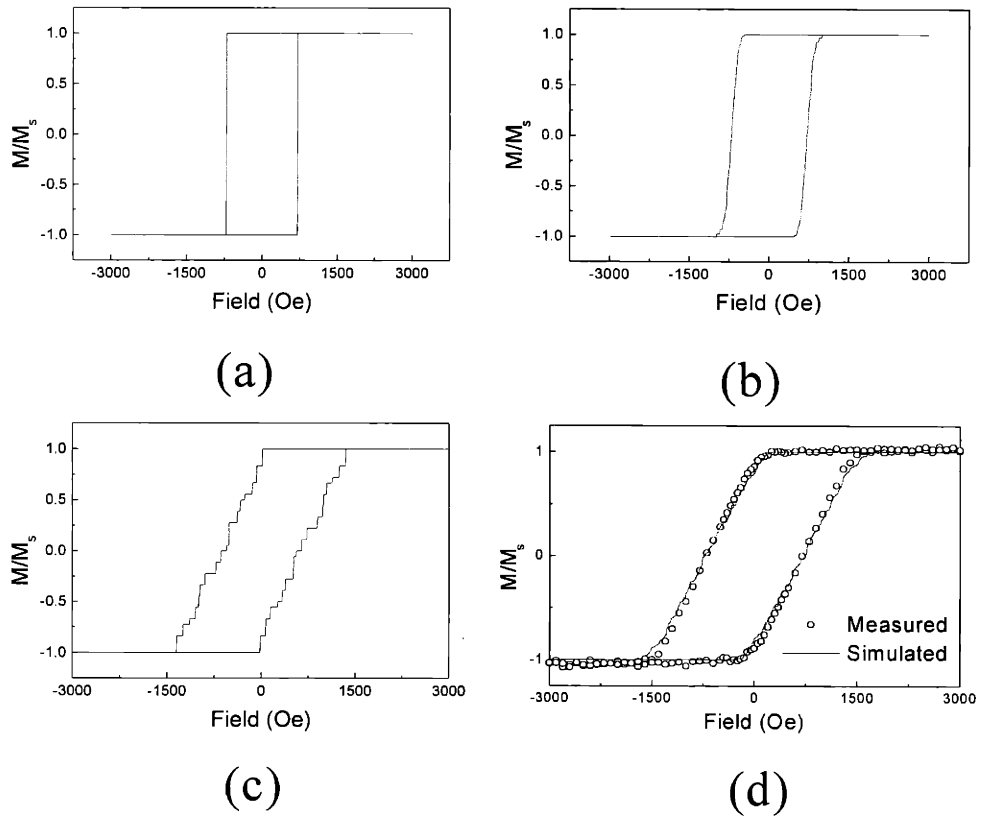

Figure 5.17: The change of hysteresis loop shape with switching field distribution and magnetostatic interaction. (a) zero ΔH_{sw} and zero magnetostatic interaction (b) zero magnetostatic interaction but nonzero ΔH_{sw} (c) zero ΔH_{sw} but including interactions (d) magnetostatic interaction combined with switching field spread

Figure 5.17 shows how the loop shape changes with each contribution. Sample Ni-01 is chosen for the comparison with the simulation results, so all the parameters are taken from measurements on sample Ni-01. As shown in Figure 5.17 (b), the spread of switching field, ΔH_{sw}, causes rounding of the loop corners and a small shear of the loop. Most of the loop shear originates from the magnetostatic interaction as shown in Figure 5.17 (c). However, if all particles have the same switching field, the hysteresis loop will show discrete jumps due to the collective switching of groups of particles. Adding the spread of

switching field to the demagnetizing magnetostatic interactions fits the experimental data quite well.

To check the validity of this parameterization for the interpretation of our Type A samples, the following test is performed. A major hysteresis loop of sample Ni-04 is fitted with the experimental data, and ΔH_{sw} = 100 Oe is obtained from the fitting. The same parameters are then used for a virgin curve simulation, and the simulated curve is compared with the experimental data. A virgin curve is simulated by starting from the saturated state and numerically AC-demagnetizing the particle array. An oscillating field of slowly decreasing amplitude is applied, and the AC demagnetized state is obtained. Starting from the AC demagnetized state, an increasing magnetic field is applied to obtain the virgin curve.

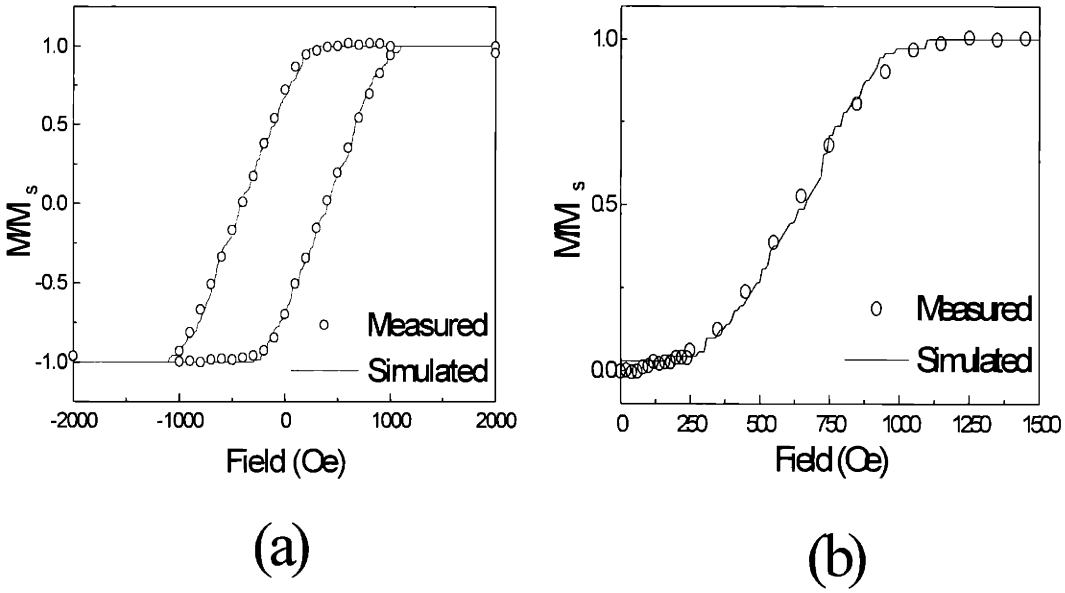

Figure 5.18: Same parameterizations are used for both (a) hysteresis loop simulation and (b) virgin curve simulation

As shown in Figure 5.18, the agreement is excellent. Thus, Type A particles can be represented quite well as magnetostatically interacting dipoles with a Gaussian distribution of switching fields.

5.6 Summary for Cylindrical Particles

From all the analysis, we have shown that the diameter of cylindrical particles must be smaller than $3.5l_{ex}$ to be single-domain flower state. This critical diameter can be increased with the help of out-of-plane anisotropy. A magnetic state diagram of remanent states was constructed for more general applications. The average switching field of these particles increases with decreasing diameter and increasing aspect ratio. However, even for particles with the same dimensions, the spread of switching field is observed and attributed to the changes in microstructure from particle to particle. Not only the geometries but also the microstructures have to be controlled to engineer the switching fields of the media. Demagnetizing magnetostatic interaction can lead to spontaneous reversals of magnetization, which means the destruction of stored data, so has to be considered well in the design of media.

5.7 Patterned Media Design

For the design of the media, we can follow the procedures described below.

1) First, we need to decide on the particle shape and aspect ratio.

2) The upper bound for particle size can be determined from the remanence study.

3) The average switching field, H_{sw}, can be computed by numerical micromagnetic simulation.

4) The optimum spacing and particle size can be computed from the condition, $H_{sw} > 9 \cdot H_i$

This procedure is demonstrated for a cylinder with an aspect ratio of 2. For generality, all parameters are normalized in the calculation. From the remanence simulations in this chapter, we know the particle should be smaller than $3.5l_{ex}$. A 5x5x10 discretization is used to compute the average switching field. The normalized switching field $H_{sw}/(4\pi M_s)$ and plotted as a function of normalized particle size in Figure 5.19. For cylindrical particles, the stability condition, $H_{sw} > 9 \cdot H_i$ can be written as a function of particle diameter and height. The normalized maximum interaction field is,

$$\frac{9H_i}{4\pi M_s} = \frac{9M_s V}{4\pi M_s p^3} = \frac{9d^2 h}{16p^3} \tag{5.4}$$

Since we are dealing with a cylinder of aspect ratio 2, h can be written as $2d$. Moreover, if we set $p=Nd$ where N is an arbitrary real number larger than 1, Equation 5.4 can be rewritten as,

$$\frac{9H_i}{4\pi M_s} = \frac{18d^3}{16p^3} = \frac{9}{8N^3} \tag{5.5}$$

This is given as a straight line parallel to the x axis in Figure 5.19. Only the regions above these lines are feasible for stable media, so it sets another limit for the particle size for a particular spacing. From this plot, we can conclude that the period of the structure has to be at least two times larger than the diameter of particles to be a stable patterned media. Although this method is only demonstrated for cylindrical particles, it can be applied to periodic square arrays of particles with any shape.

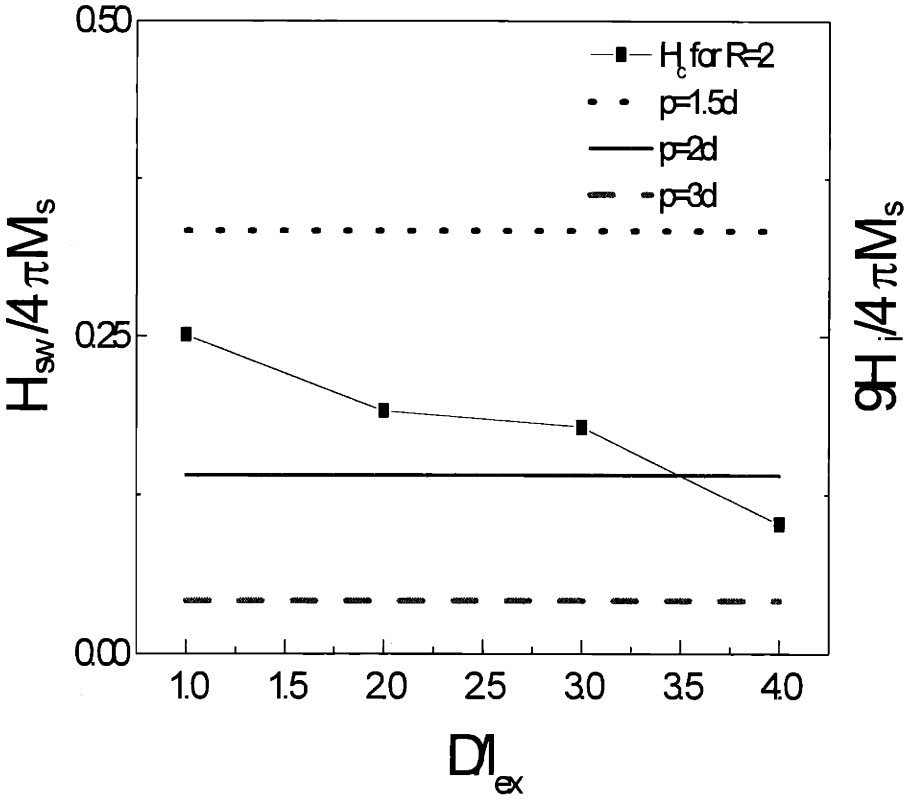

Figure 5.19: Optimum spacing engineering plot. The minimum spacing required for the stability of media can be determined by micromagnetic simulation of average switching field and the stability criteria

Chapter 6

Conclusion

In this thesis, the magnetic behavior of nanostructured ferromagnetic particle arrays are investigated using experiments and numerical micromagnetics. We have fabricated 100nm or 200nm period arrays of nanostructured Ni, Co, and CoP by the techniques of interference lithography combined with evaporation and electrodeposition. The nanomagnet arrays are characterized by bulk magnetometry and magnetic force microscopy. The remanent states of conical and cylindrical particles are studied by micromagnetic simulations and compared with experimental measurements. Depending on particle size, aspect-ratio, shape, and anisotropy, particles show either "flower" or "vortex" magnetic configurations. The critical diameter for this transition is shown to be $3.0l_{ex}$ for truncated conical particles and $3.5l_{ex}$ for cylindrical particles. For the special case of zero anisotropy, the magnetic state diagram is constructed as a function of normalized diameter and aspect ratio. The influence of uniaxial anisotropy on the remanence states is also studied.

The average switching field of particle is shown to increase with increasing aspect ratio and decreasing diameter. The origin of the experimentally observed spread in switching field for the same size particles is due to variations in the microstructure of particles. Thus, not only the particle geometry but also the microstructure of particles must be controlled for data storage applications.

The effect of demagnetizing magnetostatic interactions and switching field spread on the squareness and the shape of hysteresis loops is studied with the help of an Ising-like interaction model. The demagnetizing magnetostatic interaction is shown to be responsible for the decrease of squareness for closely packed particles, and the spread in switching fields causes rounding of the corners and small shear of the hysteresis loop. By compari-

son between the maximum magnetostatic interaction field and the average switching field, the stability criteria for patterned media is found, and the method for determination of the optimum spacing is shown by an optimum spacing engineering plot.

From the physics side, control of the spread in switching fields seems to be the most challenging barrier for the real implementation of patterned media. Although we focused on shape anisotropy controlled media in this study, flat particles with strong out-of-plane magnetocrystalline anisotropy would achieve greater data density due to weaker demagnetizing magnetostatic interaction. In this case, more stringent control of microstructure would be necessary since the switching characteristics are solely determined by microstructure. Moreover, to compete with conventional thin film media, more economic ways of fabricating periodic arrays of uniform dots have to de developed. Self-assembled particles or X-ray lithography seems to be promising technologies for production of patterned media.

Even though we focused on the recording media applications of these nanomagnet arrays, the knowledge we obtained from this study can be transferred to other types of applications utilizing nanostructured magnets such as magnetic random access memories (MRAMs), magnetic sensors, and spin transistors.

References

1 H Neal Bertram, "Theory of Magnetic Recording," p1, Cambridge University Press, New York (1994)

2 D. A. Thompson and J. S. Best, "The future of magnetic data storage technology," *IBM J. Res. Develop*, **44**(3), 311 (2000)

3 L. Bruno, "The age of petabytes," Red Herring, 266-267 (2000)

4 http://www.storage.ibm.com/technolo/grochows/grocho01.htm

5 M. Doerner, X. Bian, M. Madison, K. Tang, Q. Peng, A. Polcyn, T. Arnoldussen, Michael F. Toney, M. Mirzamaani, K. Takano, E. Fullerton, D. Margulies, M. Schabes, K. Rubin, M. Pinarbasi, S. Yuan, M. Parker, and D. Weller, "Demonstration of 35 Gbits/in2 in media on glass substrates," *IEEE Trans. Magn.*, **37**(2), 1052-1058 (2001)

6 C. A. Ross, Henry I. Smith, T. Savas, M. Schattenburg, M. Hwang, M. Walsh, M. C. Abraham, and R. J. Ram, "Fabrication of patterned media for high density magnetic storage," *J. Vac. Sci. Technol. B.*, **17**(6), 3168-3176 (1999)

7 Amikam Aharoni, "Introduction to the Theory of Ferromagnetism," Oxford University Press, New York (1996)

8 S. H. Charap and P. L. Lu, "Thermal Stability of Recorded Information at High Densities," *IEEE Trans. Magns.*, **33**(1), 978-983 (1997)

9 S. E. Lambert, I. L. Saunders, A. M. Patlach, M. T. Krounbi, and S. R. Hetzler, "Beyond discrete tracks - other aspects of patterned media," *J. Appl. Phys.*, **69**, 4724-6 (1991)

10 S. Chou, M. Wei, P. Krauss, and P. Fischer, "Single-domain magnetic pillar array of 35nm diameter and 65 Gbits/in2 desntiy for ultrahigh density quantum magnetic storage," *J. Appl. Phys.*, **76**(10), 6673-5 (1994)

11 T. L. Gilbert, "A Lagrangian Formulation of the Gyromagnetic Equation of the Magnetization field," *Phys. Rev.*, **100**, 1243 (1955)

12 L. Landau and E. Lifshitz, "On the theory of the dispersion of magnetic permeability in ferromagnetic bodies," *Physik. Z. Sowjetunion.*, **8**, 153 (1935)

13 A. Aharoni, "Elongated single-domain ferromagnetic particles", *J. Appl. Phys.*, **63**, 5879-82 (1988)

14 A. Aharoni, "The remanent state of fine particles", *IEEE Trans. Magns.*, **29**, 2596-2601 (1993)

15 A. Aharoni, "Angular dependence of nucleation by curling in a prolate spheroid", *J. Appl. Phys.*, **82**, 1281-7 (1997)

16 E. C. Stoner, F. R. S. Wohlfarth and E. P. Wolhfarth, "A mechanism of magnetic hysteresis in heterogeneous alloys," *Philo. Trans. Roy. Soc. London Ser. A*, **240**, 599 (1948)

17 Manfred E. Schabes, "Micromagnetic theory of non-uniform magnetization processes in magnetic recording particles," *J. Magn. Magn. Mat.* **95**, 249-288 (1991)

18 M. Farhoud, M. Hwang, Henry I. Smith, M. L. Schattenburg, J. M. Bae, K. Youcef-Toumi, and C. A. Ross, "Fabrication of large area nanostructured magnets by interferometric lithography", *IEEE Trans. Magns.*, **34**, 1087-1089 (1998)

19 T. A. Savas, M. Farhoud, Henry I. Smith, M. Hwang, and C. A. Ross, "Properties of large-area nanomagnet arrays with 100nm period made by interferometric lithography", *J. Appl. Phys.*, **85**(8), 6160-6162 (1999)

20 A. Fernandez, H. T. Nguyen, J. A. Britten, R. D. Boyd, M. D. Perry, D. R. Kania, and A. M. Hawryluk, "Use of interference lithography to pattern arrays of submicron resist structures for field emission flat panel displays", *J. Vac. Sci. Technol. B.*, **15**, 729 (1997)

21 A. Fernandez, J. Y. Decker, S. M. Herman, D. W. Phillion, D. W. Sweeney and M. D. Perry, "Methods for fabricating arrays of holes using interference lithography", *J. Vac. Sci. Technol. B.*, **15**(6)b 2439-43 (1997)

22 M. Farhoud, J. Ferrera, A. J. Lochtefeld, M. L. Schattenburg, C. A. Ross and H. I. Smith, "Fabrication of 200nm period nanomagnet arrays using interferometric lithography and a negative resist", *J. Vac. Sci. Technol. B.*, **17** 3182-5 (1999)

23 P. R. Krauss, P. B. Fischer, and S. Y. Chou, "Fabrication of single-domain magnetic pillar array of 35nm diameter and 65 Gbits/in^2 density", *J. Vac. Sci. Technol. B.*, **12**(6), p3639 (1994)

24 A. Brenner, "Electrodeposition of Alloys II," p457, Academic, New York (1963)

25 Y. Fukunaka, S. Aikawa, and Z. Asaki, "Fundamental-study on electrodeposition of Co and Co-P films," *J. Electrochemical Soc.*, **141**, 1783-91 (1994)

26 L. Lanotte, P. Matteazzi, and V. Tagliaferri, "Structural order and magnetism of Co-P alloys produced by electrochemical deposition," *Materials Science and Technology*, vol **6**, 146-150 (1990)

27 M. Shima, M. Hwang, M. Farhoud, T. A. Savas, A. Tzacyk, J. U. C. Parrochon, W. Escoffier, Henry I. Smith, C. A. Ross, and W. Schwarzacher, "Fabrication and magnetic properties of arrays of electrodeposited cylinders", in press, *Proc. Electrochem. Soc. Fall Mtg.* (2000)

28 E. Samwel, "Magnetic characterization of recording materials: design, instrumentation and experimental methods.", Twente, Ph.D. Thesis, University of Twente.

29 B. D. Cullity, "Introduction to Magnetic Materials", Reading, MA, Addison-Wesley.

30 J. W. Harrell, "Effect of AC gradient field on magnetic measurements with an alternating gradient magnetometer", *J. Magn. Magn. Mat.* **205**, 121-129 (1999)

31 M. Hwang, M. Abraham, T. Savas, H. Smith, R. Ram, and C. Ross, "Magnetic force microscopy study of interactions in 100 nm period nanomagnet arrays," *J. Appl. Phys.*, **87**, 1-3 (2000)

32 C.A. Ross, M. Farhoud, M. Hwang, H.I. Smith, M. Redjdal and F.B. Humphrey, "Micromagnetic behavior of conical ferromagnetic particles", *J. Appl. Phys.* **89** 1310-1319 (2000)

33 M. E. Schabes and H. N. Bertram, "Magnetization processes in ferromagnetic cubes," *J. Appl. Phys.*, **64**, 1347-57 (1988)

34 C. Seberino and H. N. Bertram, "Numerical study of hysteresis and morphology in elongated tape particles," *J. Appl. Phys.*, **85**, 5543 (1999)

35 A. Aharoni, "Upper bound to a single-domain behavior of a ferromagnetic cylinder," *J. Appl. Phys,* **68**, 2892 (1990)

36 Alex Hubert and Rudolf Schafer, "Magnetic domains" Springer-Verlag, Berlin Heigelberg (1998)

37 R. C. O'Handley, "Modern magnetic materials: principles and applications", Wiley, New York. (2000)

38 M. C.Abraham, H. Schmide, T. A. Savas, Henry I. Smith, C. A. Ross, and R. J. Ram, "Magnetic properties and interactions of single-domain nanomagnets in a periodic array", to be published

39 C. Haginoya, S. Heike, et al, "Magnetic nanoparticle array with perpendicular crystal magnetic anisotropy", *J. Appl. Phys.* **85**(12), 8327-31 (1999)

40 A. Fernandez, M. Gibbons, M. Wall, and C. Cerjan, "Magnetic domain structure and magnetization reversal in submicron-scale Co dots," *J. Magn. Magn. Mat.* **190**, 1-2 (1998)

41 K. Yu. Gusilenko, Sug-Bong Choe, and Sung-chul Shin, "Reorientational magnetic transition in high-density arrays of single-domain dots", *Appl. Phys. Letters.* **76,** 3609-3611 (2000)

42 K. Yu. Gusilenko, "Magnetostatic interdot coupling in two-dimensional magnetic dot arrays", *Appl. Phys. Letters.* **75**, 394 -396 (1999)

43 M. Hwang, M. Farhoud, Y. Hao, M. Walsh, T.A. Savas, H.I. Smith, C.A. Ross, "Major hysteresis loop modeling of two-dimensional arrays of single-domain particles", in press, *IEEE Trans. Magn.* (2000)

44 G. Zheng and M. Pardavi-Horvath, "Major loop reconstruction from switching of individual particles", *J. Appl. Phys.*, **81**, 5591-5593 (1997)

45 R. I. Joseph and E. Schlomann, "Demagnetizing field in nonellipsoidal bodies", *J. Appl. Phys.*, **36**, 1579-1593 (1965)